The Astronomical Journal, 168:235 (21pp), 2024 December https://doi.org/10.3847/1538-3881/ad7796
© 2024. The Author(s). Published by the American Astronomical Society.
OPEN ACCESS

Searching for GEMS: Characterizing Six Giant Planets Around Cool Dwarfs

Shubham Kanodia[1], Arvind F. Gupta[2], Caleb I. Cañas[3,36], Lia Marta Bernabò[4], Varghese Reji[5], Te Han[6], Madison Brady[7], Andreas Seifahrt[7], William D. Cochran[8,9], Nidia Morrell[10], Ritvik Basant[7], Jacob Bean[7], Chad F. Bender[11], Zoë L. de Beurs[12,37,38], Allyson Bieryla[13], Alexina Birkholz[14], Nina Brown[7], Franklin Chapman[14], David R. Ciardi[15], Catherine A. Clark[16,17], Ethan G. Cotter[14], Scott A. Diddams[18,19], Samuel Halverson[20], Suzanne Hawley[21], Leslie Hebb[22], Rae Holcomb[6], Steve B. Howell[23], Henry A. Kobulnicky[14], Adam F. Kowalski[24,25,26], Alexander Larsen[14], Jessica Libby-Roberts[27,28], Andrea S. J. Lin[27,28], Michael B. Lund[15], Rafael Luque[7], Andrew Monson[11], Joe P. Ninan[5], Brock A. Parker[11], Nishka Patel[29], Michael Rodruck[30], Gabrielle Ross[31], Arpita Roy[32], Christian Schwab[33], Guðmundur Stefánsson[34], Aubrie Thoms[30], and Andrew Vanderburg[35]

[1] Earth and Planets Laboratory, Carnegie Science, 5241 Broad Branch Road, NW, Washington, DC 20015, USA; skanodia@carnegiescience.edu
[2] U.S. National Science Foundation National Optical-Infrared Astronomy Research Laboratory, 950 N. Cherry Avenue, Tucson, AZ 85719, USA
[3] NASA Goddard Space Flight Center, 8800 Greenbelt Road, Greenbelt, MD 20771, USA
[4] Institute of Planetary Research, German Aerospace Center (DLR), Rutherfordstrasse 2, 12489 Berlin, Germany
[5] Department of Astronomy and Astrophysics, Tata Institute of Fundamental Research, Homi Bhabha Road, Colaba, Mumbai 400005, India
[6] Department of Physics & Astronomy, The University of California, Irvine, Irvine, CA 92697, USA
[7] Department of Astronomy & Astrophysics, University of Chicago, Chicago, IL 60637, USA
[8] McDonald Observatory and Department of Astronomy, The University of Texas at Austin, Austin, TX, USA
[9] Center for Planetary Systems Habitability, The University of Texas at Austin, Austin, TX, USA
[10] Las Campanas Observatory, Carnegie Observatories, Casilla 601, La Serena, Chile
[11] Steward Observatory, The University of Arizona, 933 N. Cherry Avenue, Tucson, AZ 85721, USA
[12] Department of Earth, Atmospheric and Planetary Sciences, Massachusetts Institute of Technology, Cambridge, MA 02139, USA
[13] Center for Astrophysics |Harvard & Smithsonian, 60 Garden Street, Cambridge, MA 02138, USA
[14] Department of Physics & Astronomy, University of Wyoming, Laramie, WY 82070, USA
[15] NASA Exoplanet Science Institute-Caltech/IPAC, Pasadena, CA 91125, USA
[16] Jet Propulsion Laboratory, California Institute of Technology, Pasadena, CA 91109, USA
[17] NASA Exoplanet Science Institute, IPAC, California Institute of Technology, Pasadena, CA 91125, USA
[18] Electrical, Computer & Energy Engineering, University of Colorado, 1111 Engineering Drive, Boulder, CO 80309, USA
[19] Department of Physics, University of Colorado, 2000 Colorado Avenue, Boulder, CO 80309, USA
[20] Jet Propulsion Laboratory, 4800 Oak Grove Drive, Pasadena, CA 91109, USA
[21] Department of Astronomy, Box 351580, University of Washington, Seattle, WA 98195, USA
[22] Department of Physics, Hobart and William Smith Colleges, 300 Pulteney Street, Geneva, NY 14456, USA
[23] NASA Ames Research Center, Moffett Field, CA 94035, USA
[24] Department of Astrophysical and Planetary Sciences, University of Colorado Boulder, 2000 Colorado Avenue, Boulder, CO 80305, USA
[25] National Solar Observatory, University of Colorado Boulder, 3665 Discovery Drive, Boulder, CO 80303, USA
[26] Laboratory for Atmospheric and Space Physics, University of Colorado Boulder, 3665 Discovery Drive, Boulder, CO 80303, USA
[27] Department of Astronomy & Astrophysics, 525 Davey Laboratory, The Pennsylvania State University, University Park, PA 16802, USA
[28] Center for Exoplanets and Habitable Worlds, 525 Davey Laboratory, The Pennsylvania State University, University Park, PA 16802, USA
[29] Maggie L. Walker Governor's School, Richmond, VA 23220, USA
[30] Department of Physics, Engineering, and Astrophysics, Randolph-Macon College, Ashland, VA 23005, USA
[31] Department of Astrophysical Sciences, Princeton University, 4 Ivy Lane, Princeton, NJ 08540, USA
[32] Astrophysics & Space Institute, Schmidt Sciences, New York, NY 10011, USA
[33] School of Mathematical and Physical Sciences, Macquarie University, Balaclava Road, North Ryde, NSW 2109, Australia
[34] Anton Pannekoek Institute for Astronomy, University of Amsterdam, Science Park 904, 1098 XH Amsterdam, The Netherlands
[35] Department of Physics and Kavli Institute for Astrophysics and Space Research, Massachusetts Institute of Technology, Cambridge, MA 02139, USA
Received 2024 June 10; revised 2024 August 16; accepted 2024 August 20; published 2024 November 4

Abstract

Transiting giant exoplanets around M-dwarf stars (GEMS) are rare, owing to the low-mass host stars. However, the all-sky coverage of TESS has enabled the detection of an increasingly large number of them to enable statistical surveys like the Searching for GEMS survey. As part of this endeavor, we describe the observations of six transiting giant planets, which include precise mass measurements for two GEMS (K2-419Ab, TOI-6034b) and statistical validation for four systems, which includes validation and mass upper limits for three of them (TOI-5218b, TOI-5616b, TOI-5634Ab), while the fourth one—TOI-5414b is classified as a "likely planet." Our observations include radial velocities from the Habitable-zone Planet Finder on the Hobby–Eberly Telescope, and MAROON-X on Gemini-North, along with photometry and high-contrast imaging from multiple ground-based

[36] NASA Postdoctoral Fellow.
[37] NSF Graduate Research Fellow.
[38] MIT Presidential Fellow, MIT Collamore-Rogers Fellow.

Original content from this work may be used under the terms of the Creative Commons Attribution 4.0 licence. Any further distribution of this work must maintain attribution to the author(s) and the title of the work, journal citation and DOI.

facilities. In addition to TESS photometry, K2-419Ab was also observed and statistically validated as part of the K2 mission in Campaigns 5 and 18, which provide precise orbital and planetary constraints despite the faint host star and long orbital period of ∼20.4 days. With an equilibrium temperature of only 380 K, K2-419Ab is one of the coolest known well-characterized transiting planets. TOI-6034 has a late F-type companion about 40″ away, making it the first GEMS host star to have an earlier main-sequence binary companion. These confirmations add to the existing small sample of confirmed transiting GEMS.

Unified Astronomy Thesaurus concepts: Extrasolar gaseous giant planets (509); Radial velocity (1332); M dwarf stars (982); Transits (1711)

Materials only available in the online version of record: machine-readable tables

1. Introduction

Transiting giant exoplanets around M-dwarf stars (GEMS) with radii $>8\ R_{\oplus}$ are rare outcomes of planet formation, with preliminary estimates of occurrence for the short-period ones (<10 days) at ∼0.1% (E. M. Bryant et al. 2023; T. Gan et al. 2023). The sample of these planets (three pre-TESS) has been bolstered by recent detections from NASA's TESS mission. Despite this, the current size of the sample (∼20) precludes robust statistical studies. Therefore, we have started the Searching for GEMS survey to provide for occurrence rates for short-period transiting GEMS across a well-characterized homogeneous sample of a million M dwarfs observed by TESS. In addition, this survey and similar community efforts (e.g., MANGOS; A. H. M. J. Triaud et al. 2023) will provide mass measurements for a large number of transiting GEMS. These mass measurements will enable a comparison of the bulk properties of these objects with their FGK short-period analogs —hot Jupiters.

GEMS likely form in an extremely mass-starved regime (S. Kanodia et al. 2023; M. Delamer et al. 2024), which raises questions as to whether this influences their present-day bulk properties or could lead to a different host star metallicity dependence (J. A. Johnson & K. Apps 2009). Beyond bulk comparisons, precise characterization of these planets enables subsequent atmospheric observations with JWST (Cycle 2 GO 3171, 3731, 4227, Cycle 3 GO 5863), as well as 3D orbital measurements through the Rossiter–McLaughlin effect (D. B. McLaughlin 1924; R. A. Rossiter 1924; S. H. Albrecht et al. 2022).

Understanding the process of giant planet formation is crucial to explain the architecture of exoplanetary systems. Studies have shown that the presence of gas giant planets affects the formation and evolution of smaller terrestrial planets both within the solar system (S. N. Raymond et al. 2009; R. Brasser et al. 2016), and in extrasolar systems (G. D. Mulders et al. 2021). In particular, close-in giant planets like transiting GEMS and hot Jupiters have confounded traditional planet formation theories (R. I. Dawson & J. A. Johnson 2018), necessitating formation farther out and then migration inward (Y. Alibert et al. 2005). Extending these giant planet samples to include cool dwarfs can enable comparisons across the stellar mass axis as a test of planet formation (and migration) models by utilizing this dependency.

In this study, we perform detailed characterization of six TESS Objects of Interest (TOIs), where we provide mass measurements for two GEMS (K2-419Ab and TOI-6034b), along with upper mass limits for four giant planets, of which two orbit M dwarfs (TOI-5616b and TOI-5634Ab) while two orbit late K dwarfs (TOI-5218b and TOI-5414b). The paper is structured as follows: In Section 2, we describe all the observations utilized in this work to validate and characterize the six planets. In Section 3, we detail the stellar characterization performed, while Section 4.2 describes the procedure followed to jointly model the data and derive planetary parameters. In Section 5, we discuss this work in the context of the existing planet sample and contextualize its importance before concluding in Section 6.

2. Observations

2.1. K2-419A

2.1.1. Photometry

K2: K2-419A (EPIC-211509553A) was observed by the Kepler spacecraft in long cadence mode (30 minute cadence) as part of Campaigns 5 and 18 during the K2 mission (Table 1). The star was originally identified as a candidate planet host by C. D. Dressing et al. (2017) and statistically validated using ground-based spectra and high-contrast imaging (J. H. Livingston et al. 2018; E. A. Petigura et al. 2018). For Campaign 18, we used the `EVEREST` pipeline (R. Luger et al. 2016, 2018) to correct for photometric variations seen in the K2 photometry due to imperfect pointing of the spacecraft with only two functioning reaction wheels. We exclude all points more than one transit duration away from each midtransit with nonzero K2 data quality flags. For Campaign 5, we find that the `EVEREST` light curves are overcorrecting the systematics outside of transit, and instead use the Campaign 5 reduced light curves from C. D. Dressing et al. (2017), which were produced following the methodology of A. Vanderburg et al. (2016). The detrended phase-folded K2 photometry (see Section 4.2 regarding detrending) is shown in Figure 1.

TESS/Presearch Data Conditioned (*PDC*) *time series light curve:* K2-419A (TOI-5176, TIC 437054764, 2MASS J09000476+1316258) was observed by TESS in Sectors 44, 45, and 46 in 2 minute cadence (Table 1). The data was processed by the TESS science processing pipeline (J. C. Smith et al. 2012; M. C. Stumpe et al. 2012, 2014; J. M. Jenkins et al. 2016), and we used the PDC time series light curves for our analysis, which were available at the Mikulski Archive for Space Telescopes (MAST). We exclude points marked as anomalous by the TESS data quality flags. The detrended phase-folded photometry for all three TESS sectors is shown in Figure 1.

0.6 m Red Buttes Observatory (*RBO*): We used the 0.6 m telescope at the RBO in Wyoming (D. H. Kasper et al. 2016) to obtain a transit for K2-419Ab on 2022 April 6. This is an $f/8.43$ Ritchey-Chrétien Cassegrain constructed by DFM Engineering, Inc. The observations were performed in the Bessell I band, with 2×2 on-chip binning and a binned plate scale of 0.″73. The observation is summarized in Table 1. The

Table 1
Summary of Ground- and Space-based Photometric Follow-up

Date UTC	Instrument	Filter	Exposure Time (s)	Median PSF FWHM (″)
K2-419A				
2015 Apr 27–2015 Jul 10	K2/C5	*Kp*	1800	...
2018 May 12–2018 Jul 2	K2/C18	*Kp*	1800	...
2021 Oct 12–2021 Nov 6	TESS/S44	*T*	120	39.5
2021 Nov 6–2021 Dec 2	TESS/S45	*T*	120	39.5
2021 Dec 2–2021 Dec 30	TESS/S46	*T*	120	39.5
2022 Apr 6	0.6 m RBO	Bessell I	240	1.58
2023 Jan 16	1.0 m Swope	SDSS *i'*	35	3.67
2024 Feb 7	0.4 m Keeble	Cousins I	180	3.51
TOI-6034				
2019 Sep 11–2019 Oct 7	TESS/S16	*T*	1800	39.5
2019 Oct 7–2019 Nov 2	TESS/S17	*T*	1800	39.5
2019 Nov 2–2019 Nov 27	TESS/S18	*T*	1800	39.5
2020 Apr 16–2020 May 13	TESS/S24*	*T*	1800	39.5
2020 May 13–2020 Jun 8	TESS/S25	*T*	1800	39.5
2022 May 18–2022 Jun 13	TESS/S52*	*T*	200	39.5
2022 Sep 1–2022 Sep 30	TESS/S56	*T*	200	39.5
2022 Sep 30–2022 Oct 29	TESS/S57	*T*	200	39.5
2022 Oct 29–2022 Nov 26	TESS/S58*	*T*	200	39.5
2023 Jun 20	0.6 m RBO	Bessell I	240	1.66
2023 Aug 8	0.6 m RBO	Bessell I	240	1.44
2023 Sep 8	0.6 m RBO	Bessell I	240	1.51
2023 Oct 9	0.4 m Keeble	Cousins I	120	5.6
2018 Mar–2022 Oct	ZTF*	ZTF *g*	30	2.5
2018 May–2023 Apr	ZTF*	ZTF *r*	30	2.5
TOI-5218				
2019 Jul 18–2019 Aug 14	TESS/S14	*T*	1800	39.5
2019 Aug 15–2019 Sep 10	TESS/S15	*T*	1800	39.5
2019 Sep 11–2019 Oct 7	TESS/S16	*T*	1800	39.5
2019 Oct 7–2019 Nov 2	TESS/S17	*T*	1800	39.5
2019 Nov 2–2019 Nov 27	TESS/S18	*T*	1800	39.5
2019 Nov 28–2019 Dec 23	TESS/S19	*T*	1800	39.5
2019 Dec 24–2020 Jan 20	TESS/S20	*T*	1800	39.5
2020 Jan 21–2020 Feb 18	TESS/S21*	*T*	1800	39.5
2020 Feb 19–2020 Mar 17	TESS/S22	*T*	1800	39.5
2020 Mar 19–2020 Apr 15	TESS/S23	*T*	1800	39.5
2020 Apr 16–2020 May 12	TESS/S24	*T*	1800	39.5
2020 May 14–2020 Jun 8	TESS/S25	*T*	1800	39.5
2020 Jun 9–2020 Jul 4	TESS/S26	*T*	1800	39.5
2021 Jun 24–2021 Jul 23	TESS/S40	*T*	600	39.5
2021 Jul 23–2021 Aug 20	TESS/S41	*T*	600	39.5
2021 Dec 30–2022 Jan 28	TESS/S47*	*T*	600	39.5
2022 Jan 28–2022 Feb 26	TESS/S48*	*T*	600	39.5
2022 Feb 26–2022 Mar 26	TESS/S49*	*T*	600	39.5
2022 Mar 26–2022 Apr 22	TESS/S50*	*T*	600	39.5
2022 Apr 22–2022 May 18	TESS/S51*	*T*	600	39.5
2022 May 18–2022 Jun 13	TESS/S52*	*T*	600	39.5
2022 Jun 13–2022 Jul 9	TESS/S53*	*T*	600	39.5
2022 Jul 9–2022 Aug 5	TESS/S54*	*T*	600	39.5
2022 Aug 5–2022 Sep 1	TESS/S55*	*T*	600	39.5
2022 Sep 1–2022 Sep 30	TESS/S56*	*T*	200	39.5
2022 Sep 30–2022 Oct 29	TESS/S57*	*T*	200	39.5
2022 Oct 29–2022 Nov 26	TESS/S58*	*T*	200	39.5
2022 Nov 26–2022 Dec 23	TESS/S59*	*T*	200	39.5
2022 Dec 23–2023 Jan 18	TESS/S60*	*T*	200	39.5
2022 May 14	3.5 m APO/ARCTIC	SDSS *i'*	20	2.8
2022 Jul 13	3.5 m APO/ARCTIC	SDSS *i'*	20	2.8
TOI-5414				
2019 Dec 24–2020 Jan 20	TESS/S20	*T*	1800	39.5
2021 Oct 12–2021 Nov 6	TESS/S44	*T*	600	39.5
2021 Nov 6–2021 Dec 2	TESS/S45	*T*	600	39.5

Table 1
(Continued)

Date UTC	Instrument	Filter	Exposure Time (s)	Median PSF FWHM (″)
2021 Dec 30–2022 Jan 28	TESS/S47	*T*	600	39.5
2022 Nov 12	0.4 m LCOGT/Teide	i'	600	2.64
TOI-5616				
2020 Feb 18–2020 Mar 18	TESS/S22	*T*	1800	39.5
2022 Jan 28–2022 Feb 26	TESS/S48	*T*	600	39.5
2022 Feb 26–2022 Mar 26	TESS/S49	*T*	600	39.5
2022 May 31	1.2 m FLWO/KeplerCam	i'	300	1.9
2018 Mar–2023 May	ZTF*	ZTF *g*	30	0.6
2018 Apr–2023 Apr	ZTF*	ZTF *r*	30	0.6
TOI-5634A				
2020 Feb 18–2020 Mar 18	TESS/S22	*T*	1800	39.5
2022 Feb 26–2022 Mar 26	TESS/S49	*T*	600	39.5
2023 Jan 5	1.2 m FLWO/KeplerCam	i'	300	2.1
2023 Mar 20	0.3 m LCRO	i'	420	1.3

Note. Instruments marked with a * are excluded from the joint analysis. We include a `tar` file containing individual `npy` binary pickled `Python` v3.9. dictionaries for each TOI created using `NumPy` v1.20. These dictionaries contain the photometry time series (including flux errors) for each instrument used in this analysis, as well as the model used for detrending where applicable. This can also be made available in other formats upon reasonable request.

(This table is available in its entirety in machine-readable form in the online article.)

astrometry for the frames was verified using the `astrometry.net` package (D. W. Hogg et al. 2008), while the aperture photometry was performed using the `photutils` package (L. Bradley et al. 2020) at the proper motion-corrected locations for all Gaia sources $G < 17$ mag. Flat, bias, and dark corrections were performed using `Astropy` (Astropy Collaboration et al. 2018). The exposure midpoints are converted to BJD_{TDB} using `barycorrpy` (S. Kanodia & J. Wright 2018), following the recommendations and algorithms from J. Eastman et al. (2010). The flux from the target star is compared to the sum of the fluxes for selected reference stars, which are present in all the frames, have no nearby companions in the aperture, and are not known variables. The final apertures are chosen to minimize the scatter in the data, while the reference stars are manually chosen to yield consistent results across all the defined apertures.

1.0 m Swope telescope: We obtained a transit of K2-419A using the 1.0 m Henrietta Swope Telescope at the Las Campanas Observatory in Chile on 2023 January 16. The Swope telescope is an f/7 Ritchey-Chrétien equipped with the E2V 4K × 4K CCD. We observed through a Sloan *i* filter. The detector was read in 2 × 2 binning mode, which yields a pixel scale of 0.″87. Only the third quadrant (C3) was used for these observations, resulting in a field of view of 14.′8 × 14.′9. The telescope was defocused in order to achieve ∼4″ full width at half-maximum (FWHM) on the images. The target was observed continuously for almost 6 hr with individual exposures of 35 s. The observation is summarized in Table 1, with data reduction and relative aperture photometry performed using `AstroImageJ` (`AIJ`; K. A. Collins et al. 2017).

0.4 m Keeble: We used the 0.4 m telescope at the Randolph-Macon College's Keeble Observatory in Ashland, Virginia, to observe a transit for K2-419A on UTC 2024 February 7. The Keeble telescope is an f/8 Ritchey-Chrétien manufactured by ASA. We used an SBIG ST-10XMEI CCD with a Kron–Cousins *I*-band filter. All observations were binned in 2 × 2 mode with a plate scale of 0.″88. Our observations for both targets are summarized in Table 1. The CCD is characterized by a gain of 1.3 e^-/ADU. Data reduction and photometric analysis were performed with `AIJ`.

2.1.2. Radial Velocity

Habitable-zone Planet Finder (*HPF*): We obtained nine visits of K2-419A with the near-infrared precision spectrograph, HPF (S. Mahadevan et al. 2012, 2014), at the 10 m Hobby–Eberly Telescope (HET; L. W. Ramsey et al. 1988). HPF is an environmentally stabilized spectrograph (G. Stefansson et al. 2016), with a stable fiber-fed illumination (S. Kanodia et al. 2018). The data is processed using the algorithms described in the `HxRGproc` package (J. P. Ninan et al. 2018), with the barycentric correction performed using `barycorrpy` (S. Kanodia & J. Wright 2018) based on the algorithms from J. T. Wright & J. D. Eastman (2014). Similar to previous observations of faint TOIs with HPF, we do not use the simultaneous calibration using the laser-frequency comb (LFC; A. J. Metcalf et al. 2019) due to concerns about scattered light from the comb, but instead interpolate the instrument wavelength solution from LFC observations taken at the beginning and end of the night, which has been shown to have a precision of ∼30 cm s^{-1} per observation (G. Stefansson et al. 2020). We calculate radial velocities (RVs) using a version of the template-matching algorithm (e.g., G. Anglada-Escude & R. P. Butler 2012) `SERVAL` (M. Zechmeister et al. 2018), which has been modified for use with HPF spectra (G. Stefansson et al. 2020, 2023). The HPF data have a median per pixel signal-to-noise ratio (S/N) per unbinned exposure (of 969 s) at 1070 nm of 18. Each of our nine visits consisted of two exposures of 969 s each, and were binned together. The HPF RVs for K2-419A are listed in Table 2. Given that K2-419A is a faint early M dwarf ($J \sim 13.36$), our HPF RVs are insufficient to provide a mass measurement.

MAROON-X: We obtained 12 visits of K2-419A with MAROON-X (A. Seifahrt et al. 2016, 2020, 2022) at Gemini-North as part of program ID GN-2023B-Q-104 (PI: Kanodia). MAROON-X is a red-optical fiber-fed precise RV spectrograph spanning 500–920 nm across two arms (blue;

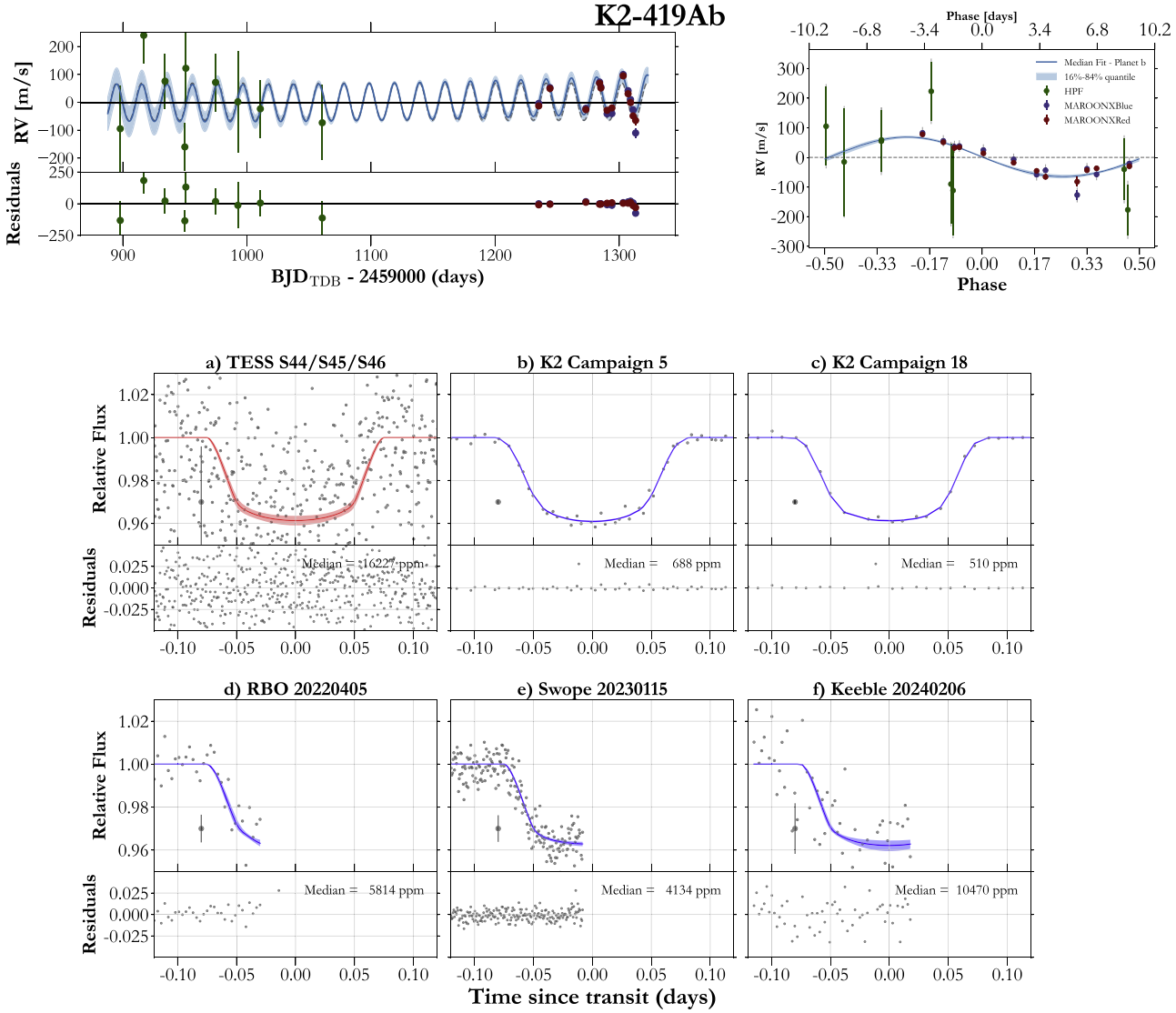

Figure 1. (Top left) RV time series for K2-419A, where the dashed line denotes the planet model, whereas the blue line and shaded region depict the best model fit (and 16%–84% uncertainties) after including the RV offsets and trends. (Top right) RVs phase folded at the best-fit period, including the model and uncertainty. The gray error bars behind the points show the errors when including the RV jitter that is estimated during the joint fit. (Bottom) Phase-folded photometry for K2-419A, including TESS (shown in red), where the dilution term is allowed to float owing to its large pixel size. The model and uncertainties follow the usual definitions. The TESS and K2 data, (a), (b), (c), are shown after subtracting the median trend as estimated after masking the planet transits. We also include the representative median statistical uncertainty at −0.07 day.

Table 2
RVs for the TOIs Included in This Paper

System	BJD$_{TDB}$ (days)	RV (m s^{-1})	σ (m s^{-1})	Instrument
K2-419A	2459897.92814	−931.16	153.49	HPF
K2-419A	2459916.87028	−596.19	98.95	HPF
K2-419A	2459934.00802	−760.52	98.52	HPF
K2-419A	2459949.96576	−996.36	85.19	HPF
K2-419A	2459950.77949	−714.25	133.49	HPF
...	...	...	...	...

Note. We show a few rows of the full table for representation purposes, while the rest of the RVs are included in a machine-readable file included with the manuscript.

(This table is available in its entirety in machine-readable form in the online article.)

500–670 nm and red; 650–920 nm) with a resolving power of ∼85,000. The wavelength solution is obtained using a Fabry–Perot etalon. Each visit consisted of a 30 minute exposure, with the 2D spectra reduced by the MAROON-X team using a custom pipeline. The RVs were estimated for each arm separately using a modified version of the SERVAL framework (M. Zechmeister et al. 2018). We treat each arm as a separate instrument, and allow for different RV offsets and jitter terms while performing a joint fit (Section 4.2). Even though our data were taken over two separate observing runs, we do not treat them as separate since the known inter-run RV offsets are known to be $\lesssim$2 m s^{-1} (A. Seifahrt et al. 2022), which is much lower than our single-visit RV uncertainty of ∼10 m s^{-1}. The MAROON-X blue and red RVs are included in Table 2, and have a median S/N per pixel in the blue and red of 18 and 29, respectively.

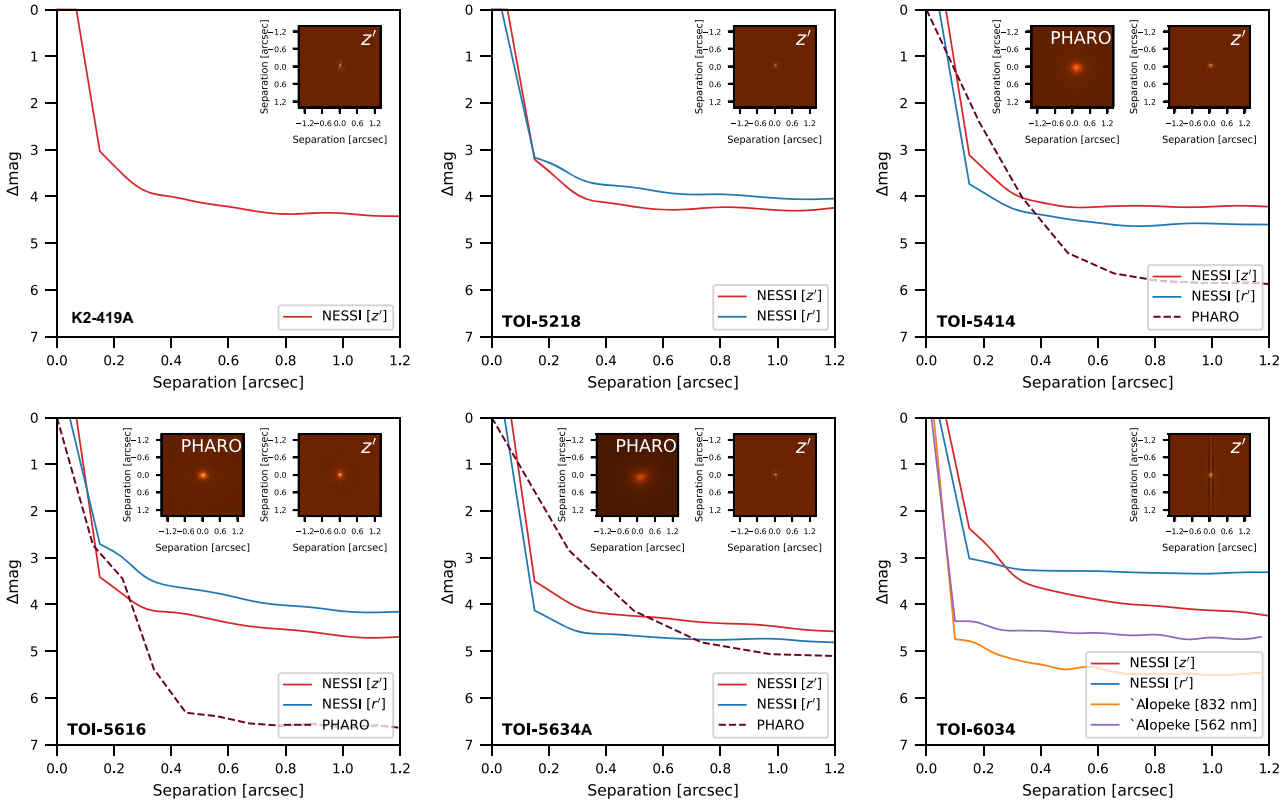

Figure 2. High-contrast imaging data for all targets. In each panel, we show the achieved 5σ contrast limit as a function of angular separation from the host star for each high-contrast data set. We also plot $1\farcs4 \times 1\farcs4$ postage stamps of the reconstructed z'-band NESSI images (right-hand inset in each panel) for all targets and the AO images (left-hand insets) for TOI-5414, TOI-5616, and TOI-5634A and TOI-6034.

2.1.3. High-contrast Imaging

To search for potential background sources, K2-419A was observed with the NN-Explore Exoplanet Stellar Speckle Imager (NESSI; N. J. Scott et al. 2018) on the WIYN[39] 3.5 m telescope at Kitt Peak National Observatory. Speckle data were taken in the Sloan Digital Sky Survey (SDSS) z' filter using the red NESSI camera on the night of 2022 April 18, and the diffraction-limited frames were then used to reconstruct a high-contrast image following the procedures described in S. B. Howell et al. (2011). The reconstructed images and 5σ contrast limits are shown in Figure 2. These data rule out the presence of any nearby sources brighter than $\Delta z' = 3.3$ mag at $0\farcs2$ and $\Delta z' = 4.4$ mag at $1\farcs2$.

2.2. TOI-6034

2.2.1. Photometry

TESS/`eleanor`: TOI-6034 (TIC 388076422, 2MASS J21113603+6824074) was observed by TESS in eight sectors, which are listed in Table 1. We extract the full frame image (FFI) data sets using `eleanor` (A. D. Feinstein et al. 2019), which uses the TESScut[40] service to obtain a cutout of 31×31 pixels. We use the `CORR_FLUX` values for the light curve, which removes correlations with respect to the pixel position, background, and the "normal" aperture mode, which uses a 3×3 pixel square aperture. Additionally, during the joint analysis, we use a Gaussian process (GP) to detrend the light curve (described in Section 4.2).

We note that TOI-6034 has a comoving companion (TIC-388076435, Gaia DR3 2270407952771897472) about $40''$ away, which causes significant contamination in the TESS light curve and is discussed in Section 3.4. This is evident in Figure 3, where we show the detrended phase-folded photometry for all the TESS sectors, with varying depths due to the large flux contamination. We discuss the procedure to correct for dilution in Section 4.2. Of the eight TESS sectors, we exclude Sectors 24, 52, and 58 from the analysis due to large systematic errors and contamination, which preclude detection of the planet transits.

0.6 m RBO and 0.4 m Keeble: We obtained three transits for TOI-6034b with the 0.6 m RBO and one with the 0.4 m Keeble observatory, which are listed in Table 1 and shown in Figure 3. For RBO and Keeble, the calibration, reduction, and relative photometry follow the same methodology as described in the preceding section for K2-419A.

Zwicky Transient Facility (*ZTF*)/`DEATHSTAR`: ZTF operates at the 1.2 m telescope at Palomar Observatory, California, and observers the entire northern sky roughly every 2 days to search for transient events (F. J. Masci et al. 2019). We use the `DEATHSTAR` (G. Ross et al. 2024) pipeline to extract 405 visits in ZTF g and 525 in ZTF r across a 4 and 5 yr baseline, respectively, with the parameters listed in Table 1. `DEATHSTAR` takes in the TIC ID of the star, downloads the ZTF data, extracts the light curves of each star in the field from the ZTF images through a custom 2D Gaussian fit, and plots the light curves for quick manual verification. Given the cadence, the

[39] The WIYN Observatory is a joint facility of the NSF's National Optical-Infrared Astronomy Research Laboratory, Indiana University, the University of Wisconsin-Madison, Pennsylvania State University, Purdue University, and Princeton University.
[40] https://mast.stsci.edu/tesscut/

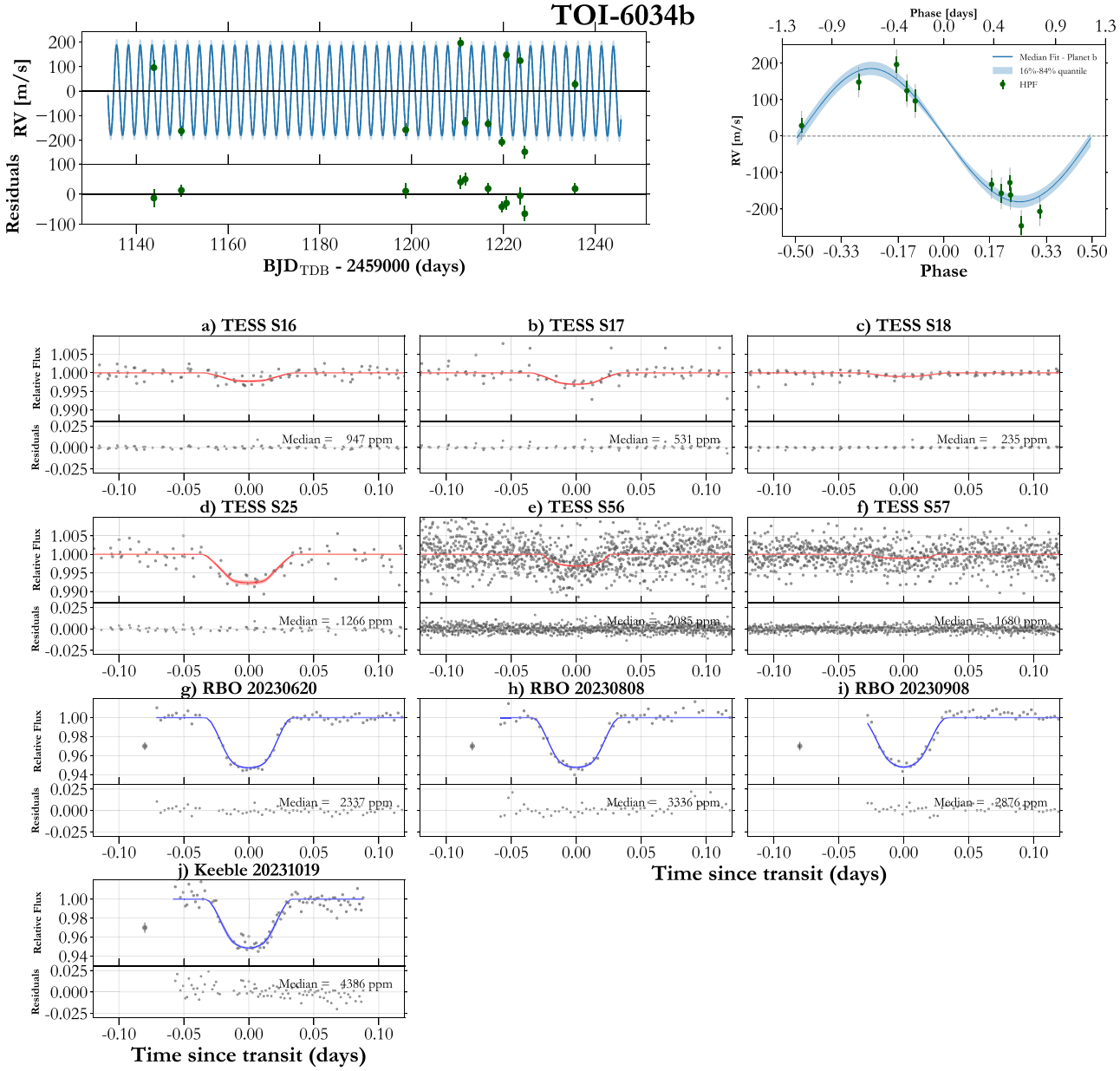

Figure 3. (Top left) RV time series for TOI-6034. (Top right) Phase-folded RVs. (Bottom) The phase-folded light curves. Note the varying TESS depths due to contamination. The plot styling and definitions are similar to Figure 1.

data is not utilized during the joint fitting (Section 4.2), but as a qualitative check to validate the host star, and is shown in Figure 4.

2.2.2. RV

We obtained 11 visits for TOI-6034 with HPF with the same exposure time and analysis protocol as detailed in Section 2.1.2 for K2-419A. The HPF spectra have a median S/N per pixel per unbinned exposure (of 969 s) at 1070 nm of 46. The HPF RVs for TOI-6034 A are listed in Table 2.

2.2.3. High-contrast Imaging

TOI-6034 was observed with NESSI on 2023 July 18. Speckle data were taken simultaneously using the red and blue NESSI cameras in the SDSS z' and r' filters, respectively. Images were reconstructed as described in Section 2.1.3. The 5σ contrast limits and the z' image are shown in Figure 2. These data rule out the presence of any nearby sources brighter than $\Delta z' = 2.7$ mag or $\Delta r' = 3.1$ mag at $0\farcs2$ and $\Delta z' = 4.2$ mag or $\Delta r' = 3.3$ mag at $1\farcs2$.

Analogous speckle data were also taken with the 'Alopeke imager (N. J. Scott et al. 2021) on the Gemini-North 8.1 m on Maunakea, using the 832 nm and 562 nm filters on the red and blue cameras. The observations were carried out on 2022 September 13, and data processing followed the same procedures described for NESSI, with which 'Alopeke shares a similar design. The 5σ contrast limits are shown in Figure 2. The 'Alopeke data rule out nearby sources to a limit of $\Delta m_{832} = 4.9$ mag or $\Delta m_{562} = 4.4$ mag at $0\farcs2$ and $\Delta m_{832} = 5.5$ mag or $\Delta m_{562} = 4.7$ mag at $1\farcs15$.

We also observed TOI-6034 with the ShARCS camera on the Shane 3 m telescope at Lick Observatory (S. Srinath et al. 2014). The target was observed on 2024 May 26 with

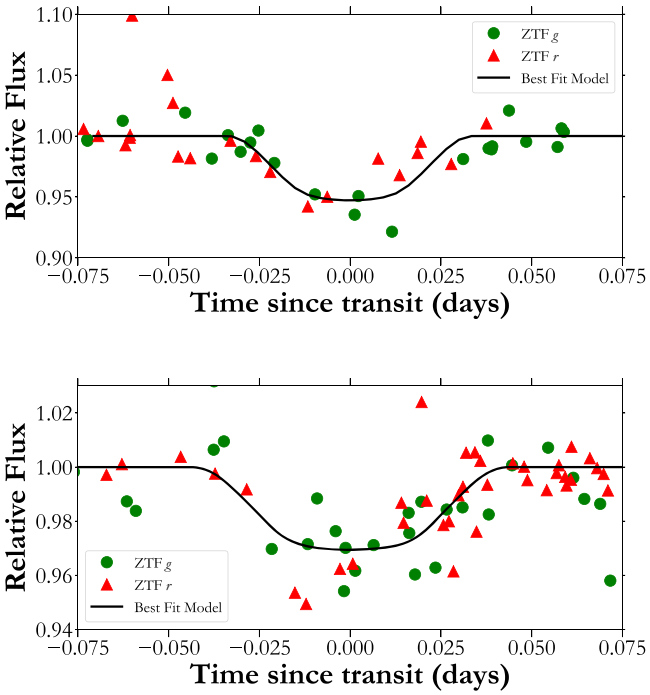

Figure 4. ZTF photometry phase folded to the best-fit planetary ephemeris, where the model is shown with a black line, and the ZTF observations in red-filled triangles (ZTF *r*) and green-filled circles (ZTF *g*). Top: observations for TOI-6034. Bottom: observations for TOI-5616.

fluctuating seeing conditions between 0.″9 and 1.″6 over the night. It was observed in Laser Guide Star mode at a single position for a total of 1500 s exposure time and then manually reduced with offset sky frames taken between exposures. We use the algorithm developed by N. Espinoza et al. (2016) to generate a 5σ contrast curve as a part of the final analysis (Figure 2). We detected no companions outside >0.″99 corresponding to a ΔK_s of 2.78, or within >1.″5 corresponding to a ΔK_s of 4.44.

2.3. TOI-5218

2.3.1. Photometry

TESS/TESS-Gaia Light Curve (`tglc`): TOI-5218 (TIC-259172249, 2MASS J19303919+7145463) was observed by TESS in 26 sectors up until year 5 of TESS observing, which are listed in Table 1. Given the need for detrending, and computational tractability, we use the first 15 sectors of TESS observations for TOI-5218. We use the `tglc` (T. Han & T. D. Brandt 2023) package to extract TESS photometry from a 3 × 3 pixel aperture, after estimating the effective point-spread function (PSF) using a 90 × 90 pixel FFI cutout. `tglc` models the PSF of all Gaia stars using a combination of Gaia positions, proper motions, and color information, which is subsequently used to remove contamination from all stars other than the target. It also removes major CCD artifacts and the gradient in the field caused by stray light.

Astrophysical Research Consortium (ARC) 3.5 m/Astrophysical Research Consortium Telescope Imaging Camera (*ARCTIC*): We observed TOI-5218 on the nights of 2022 May 13 and 2022 July 12 in SDSS *i'* using the 3.5 m ARCTIC (J. Huehnerhoff et al. 2016) at the ARC 3.5 m Telescope at Apache Point Observatory (APO). Given the presence of a background companion ∼5″ away, we defocus moderately to 2.″8 on both nights. The observations were conducted in the 4 × 4 binning mode, with a gain of 2.0 e^-/ADU, a plate scale of 0.″456 $pixel^{-1}$, and a readout time of 1.3 s. The data was calibrated and reduced using `AIJ`, and are listed in Table 1, and shown in Figure 5.

2.3.2. RV

We obtained five visits for TOI-5218 with HPF with the same exposure time and analysis protocol as detailed in Section 2.1.2 for K2-419A. The HPF spectra have a median S/N per pixel per unbinned exposure (of 969 s) at 1070 nm of 19. The HPF RVs for TOI-5218 are listed in Table 2.

2.3.3. High-contrast Imaging

TOI-5218 was observed with NESSI on 2022 September 16. Speckle data were taken simultaneously using the red and blue NESSI cameras in the SDSS z' and r' filters, respectively. Images were reconstructed as described in Section 2.1.3. The 5σ contrast limits and the z' image are shown in Figure 2. These data rule out the presence of any nearby sources brighter than $\Delta z' = 3.5$ mag or $\Delta r' = 3.3$ mag at 0.″2 and $\Delta z' = 4.2$ mag or $\Delta r' = 4.0$ mag at 1.″2.

2.4. TOI-5414

2.4.1. Photometry

TESS/`eleanor`: TOI-5414 (TIC 371164829, 2MASS J07172825+3128550) was observed by TESS in four sectors, which are listed in Table 1. We extract the photometry using `eleanor` similar to that for TOI-6034 in Section 2.2.1.

0.4 m Las Cumbres Observatory Global Telescope Network (*LCOGT*) *archival data*: We utilize a transit of TOI-5414b from the LCOGT. (T. M. Brown et al. 2013) archive, as observed on 2022 November 12 as part of proposal KEY2020B-005 (PI: Shporer, A.) from the 0.4 m Planewave Delta Rho telescope with a QHY 600 CMOS camera at the Teide Observatory in Tenerife, Spain. The observation parameters are described in Table 1, with the raw data processed by the BANZAI pipeline (C. McCully et al. 2018), and processed through `AIJ`.

2.4.2. RV

We obtained 24 visits for TOI-5414 with HPF with the same exposure time and analysis protocol as detailed in Section 2.1.2 for K2-419A. The HPF spectra have a median S/N per pixel per unbinned exposure (of 969 s) at 1070 nm of 22. The HPF RVs for TOI-5414 are listed in Table 2.

2.4.3. High-contrast Imaging

TOI-5414 was observed with NESSI on 2024 February 15. Speckle data were taken simultaneously using the red and blue NESSI cameras in the SDSS z' and r' filters, respectively. Images were reconstructed as described in Section 2.1.3. The 5σ contrast limits and the z' image are shown in Figure 2. These data rule out the presence of any nearby sources brighter than $\Delta z' = 3.4$ mag or $\Delta r' = 3.9$ mag at 0.″2 and $\Delta z' = 4.2$ mag or $\Delta r' = 4.6$ mag at 1.″2.

Observations of TOI-5414 were made on 2023 November 26 with the PHARO instrument (T. L. Hayward et al. 2001) on the Palomar Hale (5 m) behind the P3K natural guide star adaptive

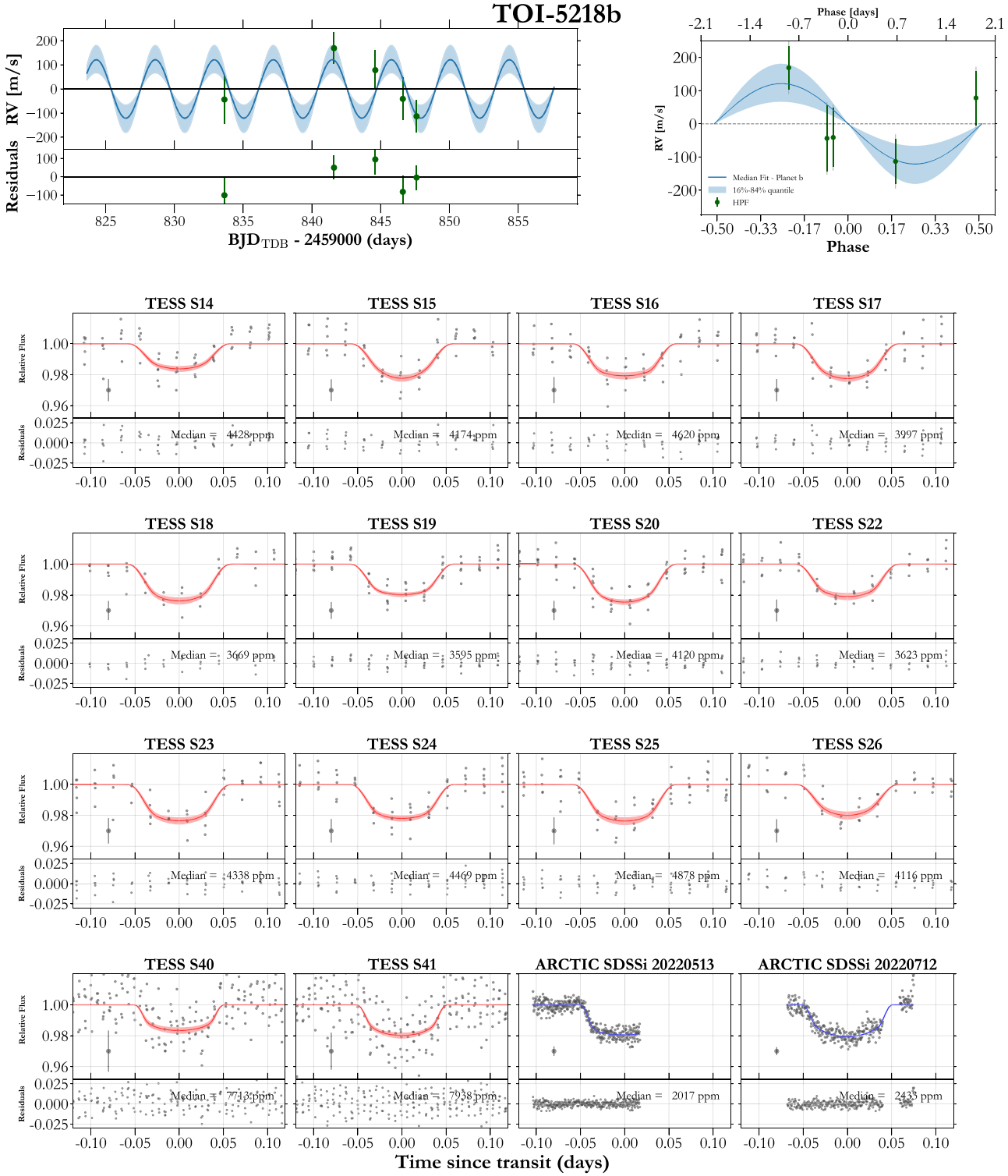

Figure 5. (Top left) RV time series for TOI-5218. (Top right) Phase-folded RVs. (Bottom) The phase-folded light curves. The plot and definitions are similar to Figure 1.

optics (AO) system (R. Dekany et al. 2013) in the narrowband $K_{\rm cont}$ filter ($\lambda_o = 2.29$; $\Delta\lambda = 0.035$ μm). The PHARO pixel scale is 0.″025 per pixel. A standard five-point dither pattern with steps of 5″ was repeated twice with each repeat separated by 0.″5. Flat fields were taken on-sky, dark-subtracted, and median averaged, and sky frames were generated from the median average of the dithered science frames. Each science image was then sky-subtracted and flat-fielded. The reduced science frames were combined into a single mosaic-ed image. The final resolution of the combined dither was determined from the FWHM of the PSF: 0.″16.

The sensitivities of the final combined AO image were determined by injecting simulated sources azimuthally around the primary target every 20° at separations of integer multiples

Table 3
Summary of Stellar Parameters for K2-419A, TOI-6034, and TOI-5218

Parameter	Description	K2-419A	TOI-6034	TOI-5218	Reference
Main identifiers:					
TOI	TESS Input Catalog Object of Interest	5176	6034	5218	TESS Input Catalog mission
TIC	TESS Input Catalog Input Catalogue	437054764	388076422	259172249	Stassun
2MASS	⋯	J09000476+1316258	J21113603+6824074	J19303919+7145463	2MASS
Gaia DR3	⋯	605593554127479936	2270404997834401664	2263568371970517120	Gaia DR3
Equatorial Coordinates, Proper Motion and Spectral Type:					
α_{J2016}	Right Ascension (RA)	135.01948 ± 0.0317	317.9001 ± 0.0149	292.6635 ± 0.0232	Gaia DR3
δ_{J2016}	Declination (Dec)	13.2737 ± 0.0232	68.4021 ± 0.0159	71.7630 ± 0.0223	Gaia DR3
μ_α	Proper motion (RA, mas/yr^{-1})	-71.336 ± 0.042	-2.430 ± 0.020	8.038 ± 0.032	Gaia DR3
μ_δ	Proper motion (Dec, mas/yr^{-1})	-27.146 ± 0.033	-5.109 ± 0.021	17.2503 ± 0.030	Gaia DR3
d	Distance in pc	263.8 ± 2.5	117.48 ± 0.22	381.4 ± 3.4	Bailer-Jones
Optical and near-infrared magnitudes:					
g'	Pan-STARRS1 g' mag	17.092 ± 0.009	15.807 ± 0.007	16.716 ± 0.018	PS1
r'	Pan-STARRS1 r' mag	15.933 ± 0.008	14.599 ± 0.005	15.498 ± 0.011	PS1
i'	Pan-STARRS1 i' mag	15.097 ± 0.008	13.672 ± 0.001	14.882 ± 0.018	PS1
z'	Pan-STARRS1 z' mag	14.732 ± 0.014	13.275 ± 0.032	14.619 ± 0.011	PS1
y'	Pan-STARRS1 y' mag	14.523 ± 0.008	13.052 ± 0.079	14.444 ± 0.009	PS1
J	J mag	...	11.901 ± 0.027	...	2MASS
H	H mag	...	11.270 ± 0.033	...	2MASS
K_s	K_s mag	...	11.016 ± 0.023	...	2MASS
$W1$	WISE1 mag	...	10.89 ± 0.02	...	WISE
$W2$	WISE2 mag	...	10.84 ± 0.02	...	WISE
$W3$	WISE3 mag	...	10.9 ± 0.07	...	WISE
G	Gaia G mag	15.7142 ± 0.0022	14.2970 ± 0.0022	15.4340 ± 0.0022	Gaia DR3
BP	BP mag	16.7499 ± 0.0056	15.4325 ± 0.0040	16.3465 ± 0.0046	Gaia DR3
RP	RP mag	14.7061 ± 0.0040	13.2556 ± 0.0031	14.5185 ± 0.0031	Gaia DR3
Spectroscopic Parameters[a]:					
$T_{\rm eff}$	Effective temperature (K)	3711 ± 88	3635 ± 88	4230 ± 88	This work
[Fe/H]	Metallicity (dex)	-0.11 ± 0.12	-0.09 ± 0.12	0.41 ± 0.12	This work
log(g)	Surface gravity (cgs units)	4.74 ± 0.05	4.77 ± 0.05	4.63 ± 0.05	This work
Model-Dependent Stellar SED and Isochrone fit Parameters[b]:					
M_*	Mass ($M_\odot$)	0.562 ± 0.024	$0.514^{+0.025}_{-0.022}$	0.739 ± 0.03	This work
R_*	Radius ($R_\odot$)	0.541 ± 0.017	$0.489^{+0.015}_{-0.014}$	0.708 ± 0.022	This work
L_*	Luminosity ($L_\odot$)	0.0529 ± 0.0024	0.0395 ± 0.0015	$0.15^{+0.009}_{-0.013}$	This work
ρ_*	Density (g/cm^3)	$4.99^{+0.42}_{-0.37}$	$6.19^{+0.45}_{-0.43}$	$2.94^{+0.25}_{-0.22}$	This work
Age	Age (Gyrs)	$7.4^{+4.4}_{-4.8}$	$7.8^{+4.2}_{-5.2}$	6.7 ± 4.4	This work
A_v	Visual Absorption (mag)	$0.066^{+0.078}_{-0.048}$	$0.131^{+0.076}_{-0.068}$	$0.51^{+0.11}_{-0.19}$	This work
Other Stellar Parameters:					
$v\sin i_*$	Proj. Rotational Velocity (km s^{-1})	< 2	< 2	< 2	This work
ΔRV	Bulk radial Velocity (km s^{-1})	-12.6 ± 0.2	9.5 ± 0.2	-9.2 ± 0.2	This work
U, V, W	Gal. Vel (barycentric, km s^{-1})	$-8.2 \pm 1.2, -4.5 \pm 0.7, -35.8 \pm 2.0$	$0.6 \pm 0.1, 10.0 \pm 0.2, 1.2 \pm 0.1$	$-31.9 \pm 0.3, -14.8 \pm 0.2, -7.0 \pm 0.1$	This work
U, V, W	Gal. Vel (LSR, km s^{-1})	$2.9 \pm 1.4, 7.8 \pm 1.0, -28.5 \pm 2.1$	$11.7 \pm 0.8, 22.2 \pm 0.7, 8.4 \pm 0.6$	$-20.8 \pm 0.9, -2.6 \pm 0.7, 0.2 \pm 0.6$	This work

Note. References are: Stassun (Burgasser 2007), 2MASS (Burgasser 2007), Gaia DR3 (Burgasser 2007), PS1 (Burgasser 2007), Bailer-Jones (Burgasser 2007), Green (Burgasser 2007), WISE (Burgasser 2007).
[a] Derived using the HPF spectral matching algorithm from Burgasser (2007).
[b] `EXOFASTv2` derived values using MIST isochrones with the GAIA parallax and spectroscopic parameters in a) as priors.

of the central source's FWHM (E. Furlan et al. 2017). The brightness of each injected source was scaled until standard aperture photometry detected it with 5σ significance. The final 5σ limit at each separation was determined from the average of all of the determined limits at that separation and the uncertainty on the limit was set by the rms dispersion of the azimuthal slices at a given radial distance. The sensitivity limits and PHARO image cutout are shown in Figure 2.

2.5. TOI-5616

2.5.1. Photometry

TESS/`tglc`: TOI-5616 (TIC-154220877, 2MASS J12193646 +4840593) was observed by TESS in three sectors, which are listed in Table 1. The planet candidate was identified in the TESS Faint Star Search (Kunimoto et al. 2022). We use `tglc` to extract the light curve from the TESS FFIs similar to that described for

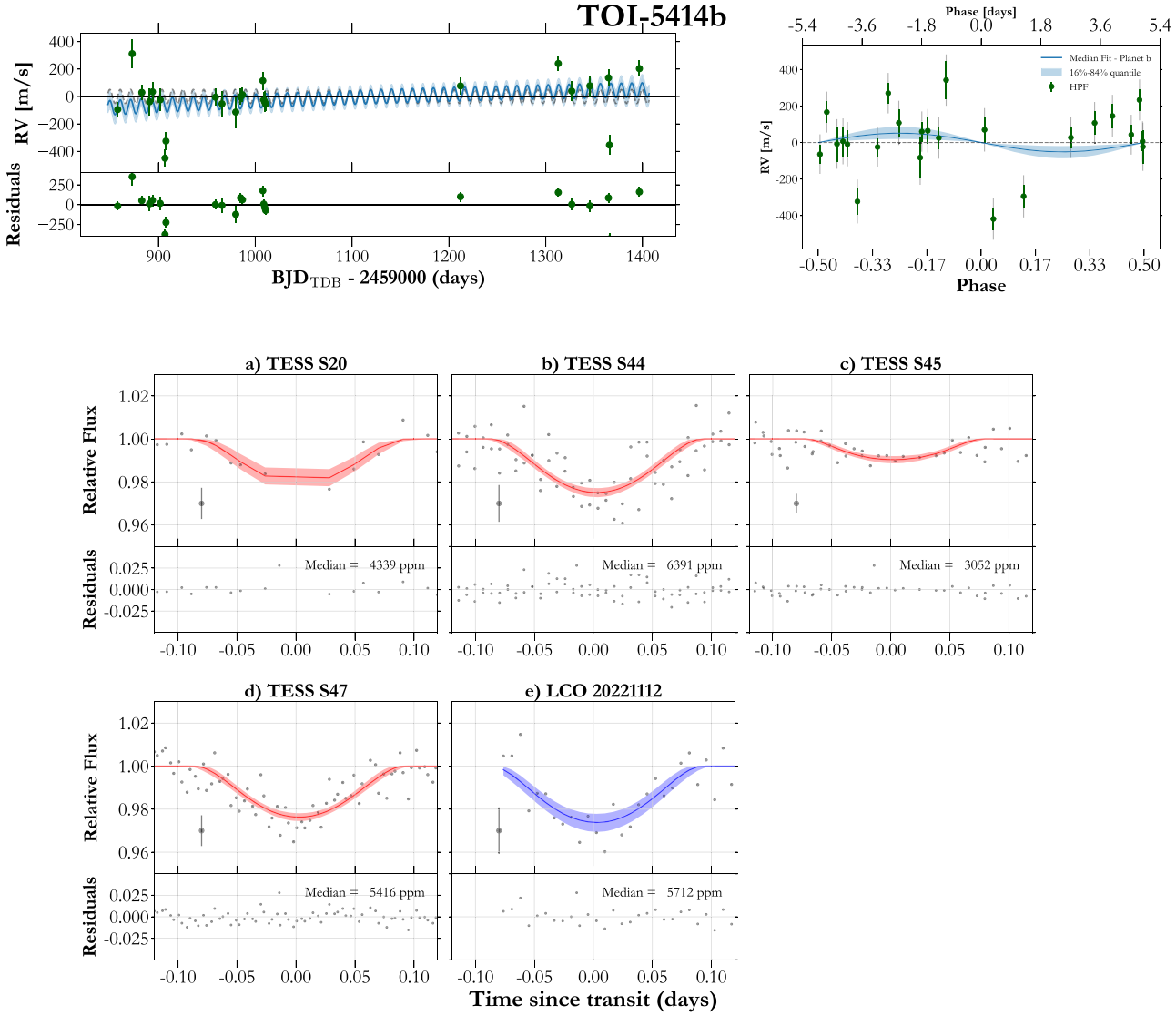

Figure 6. (Top left) RV time series for TOI-5414. (Top right) Phase-folded RVs. (Bottom) The phase-folded light curves. The plot styling and definitions are similar to Figure 1.

TOI-5218 in Section 2.3.1, while using a 31 × 31 pixel FFI cutout.

1.2 m Fred Lawrence Whipple Observatory (FLWO)/KeplerCam: We obtained a transit of TOI-5616 from KeplerCam on the 1.2 m FLWO in southern Arizona, USA (A. H. Szentgyorgyi et al. 2005) on 2022 May 31 (Table 1). It has a 4096 × 4096 Fairchild CCD with a 0.″67 plate scale per 2 × 2 binned pixel. The data was calibrated and reduced using `AIJ`, and is shown in Figure 7.

ZTF/`DEATHSTAR`: Similar to TOI-6034, we also utilize 529 visits in ZTF *g* and 568 in ZTF *r* that are listed in Table 1, and shown in Figure 4. Given the cadence, the data is not utilized during the joint fitting (Section 4.2), but as a qualitative check to validate the host star, and is shown in Figure 4.

2.5.2. RV

We obtained 12 visits for TOI-5616 with HPF with the same exposure time and analysis protocol as detailed in Section 2.1.2 for K2-419A. The HPF spectra have a median S/N per pixel per unbinned exposure (of 969 s) at 1070 nm of 19. The HPF RVs for TOI-5616 are listed in Table 2.

2.5.3. High-contrast Imaging

TOI-5616 was observed with NESSI on 2023 January 28. Speckle data were taken simultaneously using the red and blue NESSI cameras in the SDSS z' and r' filters, respectively. Images were reconstructed as described in Section 2.1.3. The 5σ contrast limits and the z' image are shown in Figure 2. These data rule out the presence of any nearby sources brighter than $\Delta z' = 3.6$ mag or $\Delta r' = 2.9$ mag at 0.″2 and $\Delta z' = 4.7$ mag or $\Delta r' = 4.2$ mag at 1.″2.

TOI-5616 was also observed with PHARO on 2024 April 22. The data were processed following the same methods described in Section 2.4.3 for TOI-5414, though with a final resolution corresponding to a PSF FWHM of 0.″11. The sensitivity limits and PHARO image cutout are shown in Figure 2.

2.6. TOI-5634A

2.6.1. Photometry

TESS/`tglc`: TOI-5634A (TIC-119585136, 2MASS J11423454 +2057553) was observed by TESS in two sectors that are listed in

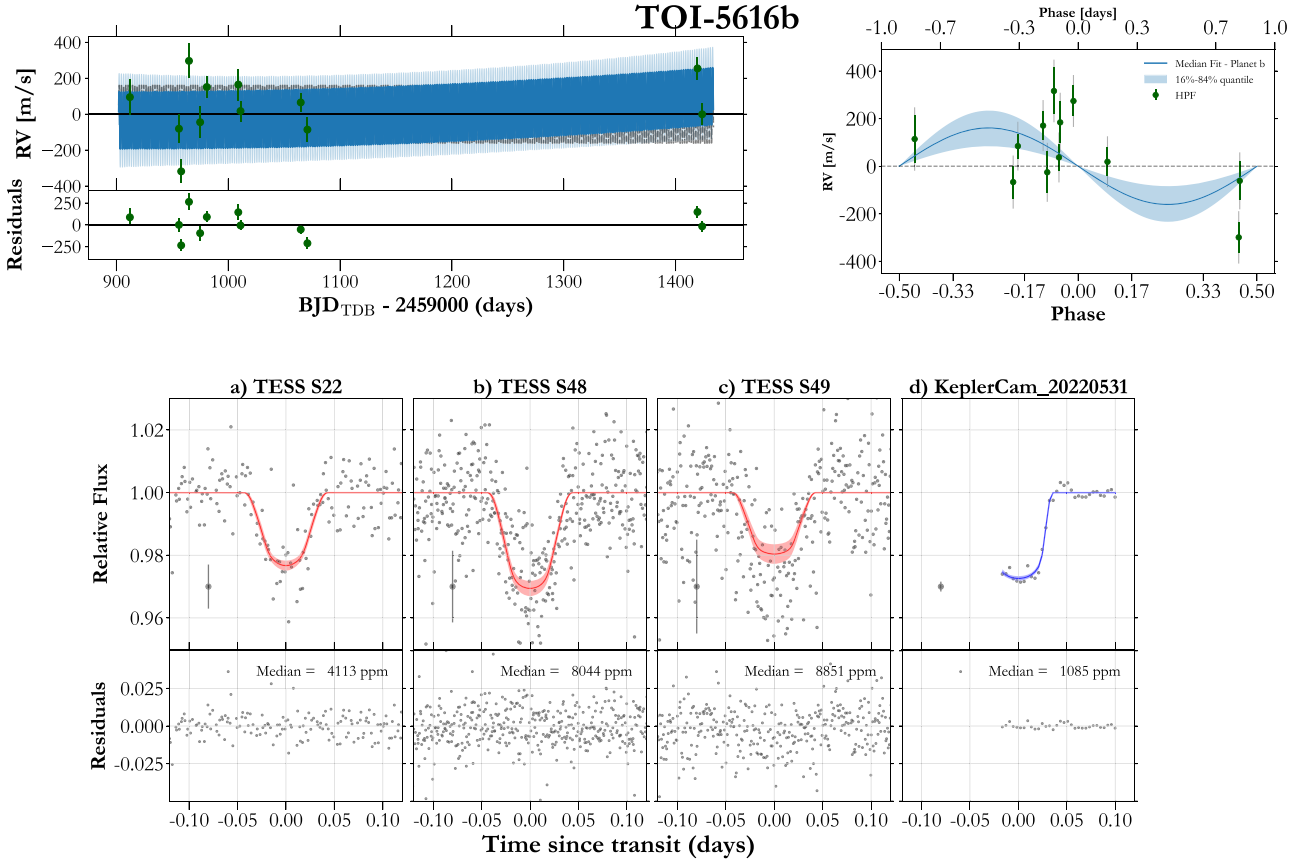

Figure 7. (Top left) RV time series for TOI-5616. (Top right) Phase-folded RVs. (Bottom) The phase-folded light curves. The plot styling and definitions are similar to Figure 1.

Table 1. We use the `tglc` package to extract the photometry similar to that for TOI-5616. The extracted, detrended, and phase-folded TESS photometry is shown in Figure 8.

1.2 m FLWO/KeplerCam: We obtained a transit of TOI-5634Ab on 2023 January 5, the details of which are included in Table 1. The data was processed using AIJ, similar to that for TOI-5616 described in Section 2.5.1.

0.3 m Las Campanas Remote Observatory (*LCRO*): We obtained a transit for TOI-5634Ab on 2023 March 20 using the 305 mm LCRO telescope at the Las Campanas Observatory in Chile. This is an f/8 Maksutov Cassegrain from Astro-Physics on a German Equatorial AP1600 GTO mount with an FLI Proline 16803 CCD Camera, FLI ATLAS Focuser, and CenterLine Filter Wheel. The data was taken unbinned, with a plate scale of 0.″773 per pixel. The data was analyzed using the same custom `Python` pipeline used with the 0.6 m RBO and described in Section 2.1.1.

2.6.2. RV

We obtained seven visits for TOI-5634A with HPF with the same exposure time and analysis protocol as detailed in Section 2.1.2 for K2-419A. The HPF spectra have a median S/N per pixel per unbinned exposure (of 969 s) at 1070 nm of 16. The HPF RVs for TOI-5634A are listed in Table 2.

2.6.3. High-contrast Imaging

TOI-5634A was observed with NESSI on 2023 January 28. Speckle data were taken simultaneously using the red and blue NESSI cameras in the SDSS z' and r' filters, respectively. Images were reconstructed as described in Section 2.1.3. The 5σ contrast limits and the z' image are shown in Figure 2. These data rule out the presence of any nearby sources brighter than $\Delta z' = 3.7$ mag or $\Delta r' = 4.3$ mag at 0.″2 and $\Delta z' = 4.6$ mag or $\Delta r' = 4.8$ mag at 1.″2.

TOI-5634A was also observed with PHARO on 2024 February 15. The data were processed following the same methods described in 2.4.3 for TOI-5414, though with a final resolution corresponding to a PSF FWHM of 0.″24. The sensitivity limits and PHARO image cutout are shown in Figure 2. This star has a detected companion 4″ to the southwest that is likely to be bound. The source (TIC 903545876 = Gaia DR3 3979511431397963008) is also detected by Gaia DR2 and DR3 and has approximately the same distance and proper motion ($d \approx 334 \pm 30$ pc; pmra $\approx -60.8 \pm 0.2$ mas yr^{-1}; pmdec $\approx -25.6 \pm 0.2$ mas yr^{-1}) as TOI-5634A. The companion star is an early/mid M dwarf (M2.5V) with a temperature of ∼3400 K; at a separation of 4″ the companion star is approximately 1300 au in projected separation. These two stars are also deemed to be a bound pair based on their Gaia astrometry by K. El-Badry et al. (2021). Based on this, we refer to the planet host as TOI-5634A.

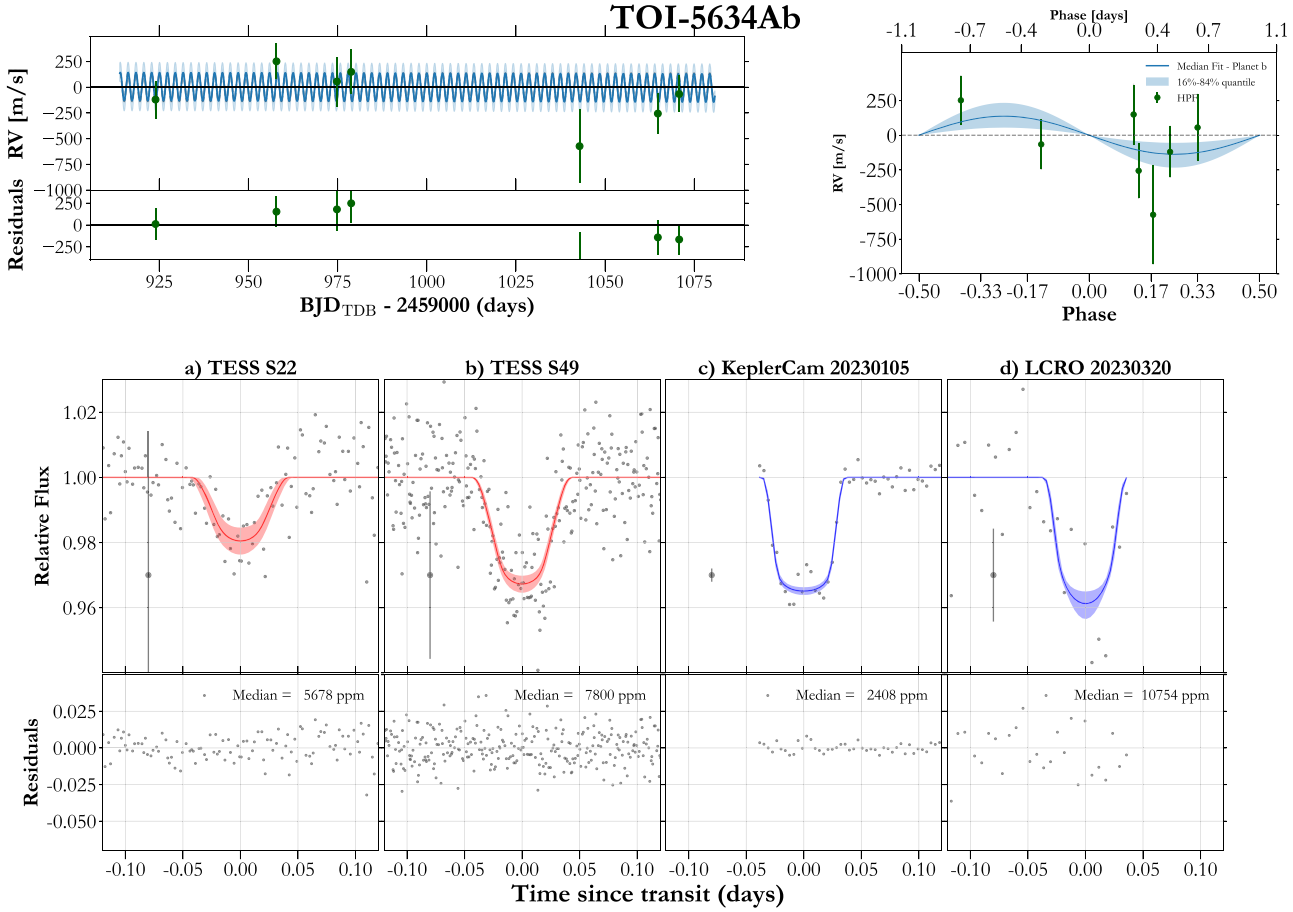

Figure 8. (Top left) RV time series for TOI-5634A. (Top right) Phase-folded RVs. (Bottom) The phase-folded light curves. The plot styling and definitions are similar to Figure 1.

3. Stellar Parameters

3.1. Spectroscopic Parameters

For all six TOIs, we first run `HPF-SpecMatch`[41] (G. Stefansson et al. 2020), to estimate $T_{\rm eff}$, $\log(g)$, and Fe/H. This is an empirical spectral matching technique which utilizes a library of HPF spectra for GKM dwarfs with well-defined labels, spanning $T_{\rm eff}$ from 2700 K to 6000 K, $\log(g)$ from 4.3 to 5.3, and Fe/H from -0.5 to $+0.5$ dex, and is adapted from `SpecMatch-Emp` (S. W. Yee et al. 2017). The target spectrum is compared with each star from the library to calculate a χ^2, which is then used to rank the top five library stars. The spectral labels for these five stars are then combined through a linear combination weighted by their relative χ^2 values. The errors on each label are estimated using a leave-one-out cross-validation process. We use HPF order index 5 for this analysis (8534–8645 Å) because it has minimal telluric contamination. Based on the χ^2 for each parameter, we caution that the recovered Fe/H estimates are not robust, and while we provide their nominal estimates for completeness, we recommend their usage only in a categorical sense (supersolar, solar, or subsolar). The spectral resolution of HPF enables us to place an upper limit of < 2 km s^{-1} for the $v \sin i_*$ of all these stars.

3.2. Model-dependent Parameters

We then use these spectroscopic parameters as priors to determine model-dependent stellar parameters by modeling the spectral energy distribution (SED) for the six TOIs using the `EXOFAST` v2 routine (J. D. Eastman 2017). The SED fit uses the precomputed bolometric corrections[42] in $\log g_\star$, $T_{\rm eff}$, [Fe/H], and A_V from the MIST model grids (J. Choi et al. 2016; A. Dotter 2016). To do this, we place Gaussian priors on the photometry specified in Tables 3 and 4 the spectroscopic parameters from `HPF-SpecMatch`, and the distance calculated from (C. A. L. Bailer-Jones et al. 2021). The spectroscopic and derived stellar parameters for all six TOIs are given in Tables 3 and 4. We note that due to the presence of nearby companions for K2-419A, and TOI-5218, we only use Pan-STARRS1 photometry (K. C. Chambers et al. 2017) to fit the SED for those two stars, whereas for the other four, we also include the Wide-field Infrared Survey Explorer (WISE; E. L. Wright et al. 2010) and Two Micron All Sky Survey (2MASS; R. M. Cutri et al. 2003). Given the faintness of all six TOIs, while we list the Gaia prism (BP, RP) magnitudes in Table 3 and 4, we do not include them in the SED fits.

3.3. UVW Velocities

We also utilize the bulk RV (derived from HPF spectra), and proper motion from Gaia DR3 (Gaia Collaboration et al. 2023),

[41] https://gummiks.github.io/hpfspecmatch/

[42] http://waps.cfa.harvard.edu/MIST/model_grids.html#bolometric

to calculate the UVW velocities in the local standard of rest (LSR; R. Schonrich et al. 2010) and barycentric frames using GALPY (J. Bovy 2015).[43] We then use the BANYAN tool (J. Gagne et al. 2018) to check the membership probabilities for each of our stars in the thin disk, thick disk, halo, or as part of moving groups. We find that all six TOIs are likely part of the thin disk as field stars.

3.4. Companion Stars

Three of our stars (K2-419A, TOI-6034, and TOI-5634A), are part of bound pairs according to the Gaia catalog from K. El-Badry et al. (2021). K2-419A has a companion (TIC-800461642, Gaia DR3 605593554127091200) $\sim 2\farcs2$ (projected separation $\sim$520 au) away that is resolved in Gaia DR3 astrometry, and at a distance of $\sim 224 \pm 21$ pc. With a G mag of 19.1, it has a $\Delta G' = 3.4$ mag, and is likely a mid/late M dwarf. Given its faintness, this companion (referred to as K2-419B from hereon) does not have a BP $-$ RP estimate. TOI-6034 also has a companion (TIC-388076435, Gaia DR3 2270407952771897472) detected in Gaia DR3 with similar proper motion and distance to TOI-6034, and at a separation of $\sim 40''$ (projected separation of $\sim$4700 A (Gaia Collaboration et al. 2023). This is a late-F star, with a G mag of 9.58 and BP $-$ RP of 0.75, with a $\Delta G' = -4.7$ mag, and causes significant contamination in the TESS light curves. TOI-5634A has an early/mid comoving M dwarf (TIC 903545876, Gaia DR3 3979511431397963008) at a separation of about $4''$ (projected separation of $\sim$1230 au) and $\Delta G' = 2.3$ mag. None of these three companion stars are close enough to the planet host stars to cause appreciable dilution in the HPF ($1\farcs7$ fiber diameter) or MAROON-X ($0\farcs77$ fiber diameter) fiber-fed spectra.

TOI-6034 is the first GEMS host to exist as part of a wide-separation binary with an earlier (FGK) main-sequence companion, while the other two join the growing list of GEMS existing in binary systems including HATS-74Ab (A. Jordan et al. 2022), TOI-3714b (C. I. Cañas et al. 2022), TOI-3984Ab (C. I. Cañas et al. 2023), TOI-5293 Ab (C. I. Cañas et al. 2023), TOI-6383Ab (M. Bernabò et al. 2024), and TOI-5688Ab (Reji et al. 2024). We will contextualize the binary separation and binary fraction of GEMS and its potential impact of giant planet formation in a future work.

4. Analysis

4.1. Validation

For all six systems, we perform a host star density check utilizing the transit duration estimate and find them consistent with the derived host star density at 1σ based on the stellar parameters (S. Seager & G. Mallen-Ornelas 2003). Additionally, while we obtained high-contrast imaging for all our targets, given the lack of mass measurements for four of them, we applied statistical validation techniques to the four planet candidates (TOI-5218b, TOI-5414b, TOI-5616b, TOI-5634Ab). We use the TRICERATOPS (S. Giacalone & C. D. Dressing 2020; S. Giacalone et al. 2021) library to statistically validate a subset of these candidates. Based on the PSF for ground-based transits for these candidates, we limit the search radius to $\sim 3''$, run 50 trials for each candidate with 1 million instances for each scenario, and include the high-contrast imaging curve as well as constraints from MOLUSC (M. L. Wood et al. 2021) utilizing the Gaia RUWE, HPF RVs, and high-contrast imaging curves. Since we have ground-based transits for each of these candidates, we set the nearby false positive probability to 0, i.e., the probability that the transit signal is from a nearby resolved star. Additionally, based on the spectra and RVs for each of these objects, we rule out the SB2 (spectroscopic binary) scenario, and set the probability of eclipsing binaries (EB) and EBx2P (EBs at twice the period) to 0. We then use the TESS light curve after detrending with GPs (described in the next section), and obtain a false positive probability (FPP) for TOI-5616b of $0.89^{+0.20}_{-0.10}\%$, for TOI-5634Ab we get $0.16^{+0.24}_{-0.05}\%$. For TOI-5218b we use the partial ARCTIC transit from 2023 May 14 and get an FPP consistent with 0 at machine precision. For TOI-5414b, we use the 0.4 m LCO photometry, which gives us an FPP of $1.9^{+0.4}_{-0.3}\%$. Based on the FPP recommendation from S. Giacalone et al. (2021), we validate TOI-5218b, TOI-5616b, and TOI-5634Ab as planets (FPP $< 1.5\%$), and TOI-5414b is likely to be a planet (FPP $< 50\%$) but not fully validated.

4.2. Joint Fitting of Photometry and RVs

We use the exoplanet (D. Foreman-Mackey et al. 2021a, 2021b) package to jointly fit the photometry with RVs. This uses pymc3 (J. Salvatier et al. 2016) to perform Hamiltonian Monte Carlo posterior estimation, starry (R. Luger et al. 2019; E. Agol et al. 2020) to model the transits, and is based on the analytical models from K. Mandel & E. Agol (2002). We use separate quadratic limb-darkening terms for each instrument. The TESS and K2 photometric data sets are detrended using a GP RotationTerm kernel, which is a combination of two simple harmonic oscillators and implemented in celerite2 (D. Foreman-Mackey et al. 2017; D. Foreman-Mackey 2018). While fitting the GP simultaneously with the transit and RV models would be ideal to prevent overfitting and provide unbiased estimates, this adds substantial computational costs. Therefore, we use a simultaneous GP term for the TESS photometry for TOI-5616 and TOI-5634, which have fewer sectors. For the other TOIs, we mask the transits and a 6 hr window on either side of each transit midpoint, and then fit a GP trend to this out-of-transit baseline, which is subsequently subtracted. This detrended light curve is then used for joint photometry + RV fitting. Due to TESS' large pixel and PSF size, we include a dilution term for each TESS sector that has a uniform prior between 0.001 and 1.5 (explained in S. Kanodia et al. 2023), and is determined using the other photometric data sets where the stars are spatially well resolved. For each RV instrument time series, we also include an RV jitter (white noise) and RV offset term while combining across instruments. For each system, we include a quadratic RV trend as a function of time ($t \cdot dv/dt + t^2 \cdot dv/dt^2$), where $t = 0$ is the mid-epoch of the RV time series.

For the two systems where we have mass measurements—K2-419Ab (Figure 1) and TOI-6034b (Figure 3), we perform a full joint fit, allowing for eccentricity to float. For the other four systems with mass upper limits—TOI-5218b (Figure 5), TOI-5414b (Figure 6), and TOI-5616b (Figure 7 and TOI-5634Ab (Figure 8)—we fix eccentricity to be circular given the few RV measurements and short orbital periods. The final derived parameters for all six systems are reported in Tables 5 and 6.

[43] With U toward the Galactic center, V toward the direction of Galactic spin, and W toward the north Galactic pole (D. R. H. Johnson & D. R. Soderblom 1987).

Table 4
Summary of Stellar Parameters for TOI-5414A, TOI-5634A, and TOI-5616

Parameter	Description	TOI-5414	TOI-5634A	TOI-5616	Reference
Main identifiers:					
TOI	TESS Input Catalog Object of Interest	5414	5634	5616	TESS Input Catalog mission
TIC	TESS Input Catalog Input Catalogue	371164829	119585136	154220877	Stassun
2MASS	⋯	J07172825+3128550	J11423454+205755	J12193646+4840593	2MASS
Gaia DR3	⋯	886990087556438784	3979511431397114752	1545570133528453888	Gaia DR3
Equatorial Coordinates, Proper Motion and Spectral Type:					
α_{J2016}	Right Ascension (RA)	109.3678 ± 0.0312	175.6436 ± 0.0436	184.9016 ± 0.0154	Gaia DR3
δ_{J2016}	Declination (Dec)	31.4818 ± 0.0278	20.9653 ± 0.0477	48.6833 ± 0.0186	Gaia DR3
μ_α	Proper motion (RA, mas/yr^{-1})	15.350 ± 0.039	-60.799 ± 0.056	-42.985 ± 0.019	Gaia DR3
μ_δ	Proper motion (Dec, mas/yr^{-1})	-22.381 ± 0.033	-25.488 ± 0.052	28.531 ± 0.025	Gaia DR3
d	Distance in pc	360.7 ± 4.3	$322.5^{+6.2}_{-5.5}$	383 ± 4.2	Bailer-Jones
Optical and near-infrared magnitudes:					
g'	Pan-STARRS1 g' mag	16.579 ± 0.007	17.311 ± 0.025	16.869 ± 0.012	PS1
r'	Pan-STARRS1 r' mag	15.401 ± 0.011	16.179 ± 0.014	15.713 ± 0.007	PS1
i'	Pan-STARRS1 i' mag	14.747 ± 0.006	15.388 ± 0.013	15.059 ± 0.014	PS1
z'	Pan-STARRS1 z' mag	14.435 ± 0.007	15.039 ± 0.007	14.775 ± 0.013	PS1
y'	Pan-STARRS1 y' mag	14.238 ± 0.017	14.857 ± 0.008	14.625 ± 0.014	PS1
J	J mag	13.136 ± 0.024	13.696 ± 0.026	13.566 ± 0.024	2MASS
H	H mag	12.486 ± 0.032	13.071 ± 0.033	12.862 ± 0.021	2MASS
K_s	K_s mag	12.287 ± 0.025	12.913 ± 0.033	12.735 ± 0.025	2MASS
$W1$	WISE1 mag	12.196 ± 0.024	12.653 ± 0.025	12.587 ± 0.023	WISE
$W2$	WISE2 mag	12.191 ± 0.023	12.615 ± 0.025	12.862 ± 0.021	WISE
$W3$	WISE3 mag	12.111 ± 0.38	12.603 ± 0.473	12.735 ± 0.025	WISE
G	Gaia G mag	15.2958 ± 0.0025	15.9859 ± 0.0024	15.6133 ± 0.0021	Gaia DR3
BP	BP mag	16.2194 ± 0.0052	16.9875 ± 0.0114	16.5177 ± 0.0039	Gaia DR3
RP	RP mag	14.3592 ± 0.0036	14.9995 ± 0.0049	14.6887 ± 0.0030	Gaia DR3
Spectroscopic Parameters[a]:					
$T_{\rm eff}$	Effective temperature (K)	4101 ± 88	3896 ± 88	3996 ± 88	This work
[Fe/H]	Metallicity (dex)	0.02 ± 0.12	-0.27 ± 0.12	0.14 ± 0.12	This work
log(g)	Surface gravity (cgs units)	4.69 ± 0.05	4.73 ± 0.05	4.67 ± 0.05	This work
Model-Dependent Stellar SED and Isochrone fit Parameters[b]:					
M_*	Mass ($M_\odot$)	$0.706^{+0.029}_{-0.025}$	0.556 ± 0.022	0.666 ± 0.025	This work
R_*	Radius ($R_\odot$)	0.691 ± 0.018	$0.540^{+0.017}_{-0.016}$	0.646 ± 0.017	This work
L_*	Luminosity ($L_\odot$)	$0.1295^{+0.0061}_{-0.0054}$	$0.0569^{+0.0028}_{-0.0024}$	0.1017 ± 0.0038	This work
ρ_*	Density (g/cm^3)	$3.02^{+0.23}_{-0.21}$	$4.99^{+0.39}_{-0.36}$	$3.49^{+0.26}_{-0.23}$	This work
Age	Age (Gyrs)	$7.2^{+4.4}_{-4.6}$	$7.4^{+4.5}_{-4.7}$	$7.2^{+4.4}_{-4.5}$	This work
A_v	Visual Absorption (mag)	$0.083^{+0.088}_{-0.058}$	$0.039^{+0.032}_{-0.027}$	0.05 ± 0.045	This work
Other Stellar Parameters:					
$v\sin i_*$	Proj. Rotational Velocity (km s^{-1})	< 2	< 2	< 3	This work
ΔRV	Bulk radial Velocity (km s^{-1})	-46.3 ± 0.2	-22.4 ± 0.2	−7.1 ± 0.2	This work
U, V, W	Gal. Vel (barycentric, km s^{-1})	52.1 ± 0.2, −39.5 ± 0.8,-4.7 ± 0.2	−57.3 ± 1.9,-64.6 ± 2.2, −49.6 ± 0.9	-90.1 ± 1.4,3.6 ± 0.1, −35.8 ± 0.5	This work
U, V, W	Gal. Vel (LSR, km s^{-1})	63.2 ± 0.9, −27.2 ± 1.0,2.5 ± 0.6	-46.2 ± 2.1,−52.4 ± 2.3, -42.3 ± 1.1	-79.0 ± 1.6,15.8 ± 0.7, −28.6 ± 0.8	This work

Note. References are: Stassun (Burgasser 2007), 2MASS (Burgasser 2007), Gaia DR3 (Burgasser 2007), PS1 (Burgasser 2007), Bailer-Jones (Burgasser 2007), Green (Burgasser 2007), WISE (Burgasser 2007).
[a] Derived using the HPF spectral matching algorithm from Burgasser (2007).
[b] `EXOFASTv2` derived values using MIST isochrones with the GAIA parallax and spectroscopic parameters in *a*) as priors.

5. Discussion

TESS has contributed to the discovery of many short-period giant exoplanets with targeted surveys such as our Searching for GEMS survey (S. Kanodia et al. 2024) geared toward M-dwarf hosts, and the TESS Grand Unified Hot Jupiter Survey (S. W. Yee et al. 2022) focused on nearby brighter FGK stars. This has led to an increasing number of giant planets orbiting brighter hosts, more amenable to detailed characterization, compared to the Kepler mission.

In particular, the sample of confirmed transiting GEMS has grown from less than a handful to about 20 confirmed planets, with many more being added by our survey. The six planets discussed in this manuscript are contextualized with respect to the existing sample of planets (NASA Exoplanet Archive 2024) in Figure 9. We discuss some salient features of the systems here.

K2-419Ab is one of the longest period GEMS (∼20 days; Figure 9) after TOI-1899 b (∼29 days; C. I. Cañas et al. 2020; A. S. J. Lin et al. 2023). Also similar to TOI-1899 b, despite

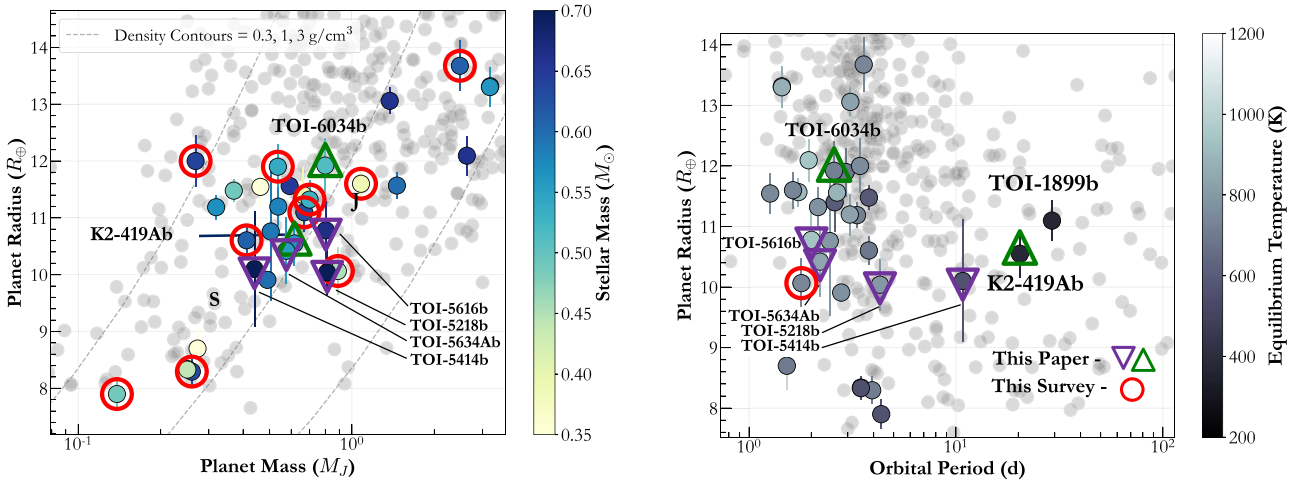

a) Planet radius as a function of mass b) Planet radius as a function of orbital period

Figure 9. We show a sample of planets with host star $T_{\rm eff} < 7200$ K, and planetary radii between 8 and 15 $R_\oplus$. In (a) and (b), we highlight systems with $T_{\rm eff} < 4300$ K to focus on the cooler host stars. In all these plots, the systems discovered as part of the Searching for GEMS are circled in red, while the TOIs confirmed here with triangles in green (upright for TOIs with mass measurements) and purple (inverted for TOIs with mass upper limits).

Table 5
Derived Parameters for the K2-419A and TOI-6034 System

Parameter	Units	K2-419A[a]	TOI-6034[a]
Orbital parameters			
Orbital period	P (days)	$20.35847252^{+0.00000614}_{-0.00000575}$	2.576184 ± 0.000002
Eccentricity	e	$0.042^{+0.045}_{-0.029}$; ($e_{<97.5\%} < 0.147$)	$0.040^{+0.042}_{-0.028}$; ($e_{<97.5\%} < 0.133$)
Argument of periastron	ω (radians)	$0.017^{+1.022}_{-1.214}$	$-0.59^{+1.75}_{-1.31}$
Semi-amplitude velocity	K (m s^{-1})	67^{+5}_{-4}	184 ± 16
Systemic velocity[b]	$\gamma_{\rm HPF}$ (m s^{-1})	-836 ± 54	6 ± 15
	$\gamma_{\rm M-Xblue}$ (m s^{-1})	-16 ± 24	...
	$\gamma_{\rm M-Xred}$ (m s^{-1})	-19 ± 23	...
RV trend	dv/dt (m s^{-1} yr^{-1})	$27.28^{+66.43}_{-67.20}$	$-15.5^{+82.1}_{-85.6}$
	dv/dt^2 (m s^{-1} yr^{-2})	$37.40^{+69.42}_{-71.57}$	-0.5 ± 95.5
RV jitter	$\sigma_{\rm HPF}$ (m s^{-1})	$49.3^{+32.5}_{-33.0}$	$35.5^{+15.9}_{-11.9}$
	$\sigma_{\rm MXblue}$ (m s^{-1})	$18.4^{+7.8}_{-5.8}$	...
	$\sigma_{\rm MXred}$ (m s^{-1})	$6.7^{+4.7}_{-3.9}$	...
Transit parameters			
Transit midpoint	T_C (BJD$_{\rm TDB}$)	2459553.7138 ± 0.0005	2459883.9055 ± 0.0003
Scaled radius	R_p/R_*	$0.1805^{+0.0031}_{-0.0028}$	$0.2233^{+0.0051}_{-0.0052}$
Scaled semimajor axis	a/R_*	$48.46^{+1.53}_{-1.40}$	$12.95^{+0.41}_{-0.37}$
Impact parameter	b	$0.389^{+0.075}_{-0.103}$	$0.674^{+0.035}_{-0.040}$
Orbital inclination	i (deg)	$89.54^{+0.12}_{-0.09}$	$87.06^{+0.22}_{-0.21}$
Transit duration	T_{14} (days)	$0.1489^{+0.0041}_{-0.0037}$	$0.0648^{+0.0019}_{-0.0020}$
Planetary parameters			
Mass	M_p ($M_\oplus$)	196 ± 15	254 ± 24
	M_p (M_J)	0.617 ± 0.047	0.798 ± 0.075
Radius	R_p ($R_\oplus$)	10.55 ± 0.39	11.92 ± 0.48
	R_p (R_J)	0.941 ± 0.034	1.063 ± 0.042
Density	ρ_p (g cm^{-3})	$0.916^{+0.136}_{-0.114}$	$0.82^{+0.14}_{-0.12}$
Semimajor axis	a (au)	$0.1208^{+0.0016}_{-0.0017}$	$0.02949^{+0.00043}_{-0.00044}$
Average incident flux[c]	$\langle F \rangle$ (10^5 W m^{-2})	0.045 ± 0.005	0.587 ± 0.068
Planetary insolation	S ($S_\oplus$)	3.3 ± 0.4	43 ± 5
Equilibrium temperature[d]	$T_{\rm eq}$ (K)	377 ± 11	714 ± 21

Notes.
[a] The reported values refer to the 16th-50th-84th percentiles of the posteriors.
[b] In addition to the "absolute RV" from Table 3.
[c] We use a solar flux constant = 1360.8 W m^{-2} to convert insolation to incident flux.
[d] We assume the planet to be a blackbody with zero albedo and perfect energy redistribution to estimate the equilibrium temperature.

Table 6
Derived Parameters for the TOI-5414, TOI-5616, TOI-5634A, and TOI-5218 Systems

Parameter	Units	TOI-5414	TOI-5616	TOI-5634A	TOI-5218
Orbital parameters					
Orbital period	P (days)	$10.778918^{+0.000089}_{-0.000092}$	2.002849±0.000004	2.2035373 ± 0.0000084	4.291452 ± 0.000004
Eccentricity	e		0 (fixed)		
Argument of periastron	ω (deg)		90 (fixed)		
Semi-amplitude velocity	K (m s^{-1})	51^{+35}_{-32}	161^{+73}_{-77}	137^{+96}_{-82}	121^{+59}_{-54}
	<97.5%; <99.85% (m s^{-1})	< 122; < 164	< 305; < 384	< 330; < 439	< 242; < 309
Systemic velocity[a]	$\gamma_{\rm HPF}$ (m s^{-1})	114 ± 35	−188 ± 50	−380 ± 77	−515±42
RV trend	dv/dt (m s^{-1} yr^{-1})	85 ± 42	92 ± 58	−29 ± 97	−0.5 ± 99.4
	dv/dt^2 (m s^{-1} yr^{-2})	-30^{+83}_{-85}	62 ± 93	−2 ± 95	0.5±100
RV jitter	$\sigma_{\rm HPF}$ (m s^{-1})	96^{+3}_{-6}	89^{+8}_{-14}	49 ± 34	46 ± 34
Transit parameters					
Transit midpoint	T_C (BJD$_{\rm TDB}$)	$2459529.1387^{+0.0028}_{-0.0025}$	2458901.48892 ± 0.00129	2459663.4184 ± 0.0011	$2458842.65207^{+0.00076}_{-0.00079}$
Scaled radius	R_p/R_*	$0.1333^{+0.0136}_{-0.0125}$	$0.1532^{+0.0047}_{-0.0044}$	0.177 ± 0.006	0.130 ± 0.002
Scaled Semimajor Axis	a/R_*	$26.29^{+0.73}_{-0.71}$	$10.21^{+0.32}_{-0.34}$	$10.85^{+0.41}_{-0.44}$	14.56 ± 0.43
Impact parameter	b	$0.21^{+0.17}_{-0.15}$	$0.34^{+0.12}_{-0.18}$	$0.36^{+0.12}_{-0.18}$	$0.40^{+0.06}_{-0.08}$
Orbital Inclination	i (deg)	$89.54^{+0.32}_{-0.37}$	$88.13^{+1.05}_{-0.73}$	$88.19^{+0.94}_{-0.69}$	$88.41^{+0.35}_{-0.30}$
Transit duration	T_{14} (days)	$0.1441^{+0.0049}_{-0.0051}$	0.0690 ± 0.0019	$0.0697^{+0.0015}_{-0.0014}$	$0.0991^{+0.0013}_{-0.0012}$
Planetary parameters					
Mass	M_p ($M_\oplus$)	140^{+96}_{-87}	255^{+118}_{-122}	183^{+129}_{-110}	254^{+125}_{-114}
	<97.5% ; <99.85% ($M_\oplus$)	< 336; < 447	< 485; < 624	<440 ; <588	< 511; < 657
Radius	R_p ($R_\oplus$)	$10.10^{+1.07}_{-0.96}$	$10.78^{+0.54}_{-0.47}$	$10.42^{+0.62}_{-0.55}$	9.86 ± 0.39
	R_p (R_J)	$0.901^{+0.095}_{-0.085}$	$0.961^{+0.048}_{-0.042}$	$0.923^{+0.056}_{-0.050}$	0.879 ± 0.034
Semimajor axis	a (au)	$0.0850^{+0.0010}_{-0.0011}$	0.0272 ± 0.0003	0.0272 ± 0.0003	0.0469 ± 0.0006
Average incident Flux[b]	$\langle F \rangle$ (10^5 W m^{-2})	0.231 ± 0.023	1.87 ± 0.08	1.05 ± 0.05	0.85 ± 0.09
Planetary insolation	S ($S_\oplus$)	17.00 ± 1.75	137 ± 6	77 ± 5	62 ± 6
Equilibrium temperature[c]	$T_{\rm eq}$ (K)	566 ± 15	939 ± 27	837 ± 34	783 ± 21

Notes.
[a] In addition to the absolute RV from Table 3.
[b] We use a solar flux constant = 1360.8 W m^{-2} to convert insolation to incident flux.
[c] We assume the planet to be a blackbody with zero albedo and perfect energy redistribution to estimate the equilibrium temperature.

having a large a/R_* of ∼48, its orbit is consistent with circular at 1.5σ. This agrees with the behavior seen by R. I. Dawson & R. A. Murray-Clay (2013), where metal-rich stars tend to host warm/cold Jupiters spanning a range of eccentricities, whereas relatively metal-poorer host stars tend to harbor more low-eccentricity warm Jupiters. K2-419A does not have rotational broadening or a rotation signal in the spectroscopic activity indicators. This conforms with studies of hot/warm/cold Jupiter samples by B. Banerjee et al. (2024), which find that warm and cold Jupiters are preferentially around old and relatively metal-poor stars.

The equilibrium temperature for K2-419Ab at ∼380 K also makes it one of the coolest giant planets with precise mass and radius measurements. In particular, planets cooler than 500 K are conducive for detection of ammonia (NH_3; K. Ohno & J. J. Fortney 2023), which can be used a tracer for the nitrogen abundance in the planetary atmosphere. In combination with carbon measured using carbon-bearing species such as carbon mono-oxide and methane, estimates of carbon, oxygen, and nitrogen can be used to make a first attempt toward reconciling the volatile content of mature exoplanet atmospheres with theories that predict volatile depletion (J. J. Lissauer 2007; F. J. Ciesla et al. 2015) and recent JWST MIRI protoplanetary disk observations; where the latter find a diverse set of conditions at these orbital separations in M-dwarf disks (E. F. van Dishoeck et al. 2023; R. Franceschi et al. 2024). A similar temperature around a solar analog necessitates a separation of 0.55 au from its host star (or a period of ∼150 days), which hampers transit observability and results in a long transit duration.

TOI-5414b (and TOI-5616b) suggest the presence of a linear (and quadratic) RV trend (Table 6). However, given the large uncertainties in the RV errors for these faint stars, as well as the large posterior width of the inferred RV trend, we advise caution in interpreting these potential trends.

6. Summary

In this manuscript, we describe the observations and analysis utilized to confirm five planets, which include mass measurements for two planets (K2-419Ab and TOI-6034b), statistical validation, and upper limits for three TOIs (TOI-5218b, TOI-5616b, and TOI-5634Ab), and the classification of TOI-5414b as a likely planet. Two of these are mid/late K dwarfs (TOI-5414b and TOI-5218b), while the rest are GEMS as part of our Searching for GEMS survey. Interestingly, of the four GEMS TOIs, three form part of binary systems, which adds to the growing sample of confirmed GEMS that exist in binary systems. K2-419Ab, which was observed with K2 and TESS

photometry, along with HPF and MAROON-X RVs is one of the coolest transiting giant planets with precise characterization. TOI-6034 hosts a transiting giant planet, and is the only one so far to have an early (F-type) main-sequence binary companion. These two planets, along with the other four TOIs with mass upper limits contribute to future statistical analysis to ascertain the possible presence of a trend between giant planet mass and stellar mass.

Acknowledgments

S.K. would like to thank the referee for their detailed comments and suggestions, which have helped improve this manuscript.

S.K. would like to thank Peter Gao for help with the computing resources that enabled running some of these memory-intensive analyses.

C.I.C. acknowledges support by NASA Headquarters through an appointment to the NASA Postdoctoral Program at the Goddard Space Flight Center, administered by ORAU through a contract with NASA.

The Pennsylvania State University campuses are located on the original homelands of the Erie, Haudenosaunee (Seneca, Cayuga, Onondaga, Oneida, Mohawk, and Tuscarora), Lenape (Delaware Nation, Delaware Tribe, Stockbridge-Munsee), Shawnee (Absentee, Eastern, and Oklahoma), Susquehannock, and Wahzhazhe (Osage) nations. As a land grant institution, we acknowledge and honor the traditional caretakers of these lands and strive to understand and model their responsible stewardship. We also acknowledge the longer history of these lands and our place in that history.

These results are based on observations obtained with the Habitable-zone Planet Finder Spectrograph on the HET. We acknowledge support from NSF grants AST-1006676, AST-1126413, AST-1310885, AST-1310875, ATI 2009889, ATI-2009982, AST-2108512, AST-2108801, and the NASA Astrobiology Institute (NNA09DA76A) in the pursuit of precision RVs in the near-infrared. The HPF team also acknowledges support from the Heising-Simons Foundation via grant 2017-0494. The Low Resolution Spectrograph 2 (LRS2) was developed and funded by the University of Texas at Austin McDonald Observatory and Department of Astronomy and by Pennsylvania State University. We thank the Leibniz-Institut für Astrophysik Potsdam (AIP) and the Institut für Astrophysik Göttingen (IAG) for their contributions to the construction of the integral field units. The Hobby–Eberly Telescope is a joint project of the University of Texas at Austin, the Pennsylvania State University, Ludwig-Maximilians-Universität München, and Georg-August Universität Gottingen. The HET is named in honor of its principal benefactors, William P. Hobby and Robert E. Eberly. The HET Collaboration acknowledges the support and resources from the Texas Advanced Computing Center. We thank the Resident astronomers and Telescope Operators at the HET for the skillful execution of our observations with HPF. We would like to acknowledge that the HET is built on indigenous land. Moreover, we would like to acknowledge and pay our respects to the Carrizo & Comecrudo, Coahuiltecan, Caddo, Tonkawa, Comanche, Lipan Apache, Alabama-Coushatta, Kickapoo, Tigua Pueblo, and all the American Indian and Indigenous peoples and communities who have been or have become a part of these lands and territories in Texas, here on Turtle Island.

Observations obtained with the APO 3.5 m telescope, owned and operated by the ARC. We acknowledge support from NSF grants AST-1910954, AST-1907622, AST-1909506, and AST-1909682 for the ultra-precise photometry effort.

This work makes use of observations (proposal ID: KEY2020B-005) from the Sinistro imaging camera on the 1 m Dome B telescope at Cerro Tololo Inter-American Observatory, operated by the LCOGT.

D.R.C. and C.A.C. acknowledge partial support from NASA grant 18-2XRP18_2-0007. This research has made use of the Exoplanet Follow-up Observation Program (ExoFOP; NExScI 2022) website, which is operated by the California Institute of Technology, under contract with the National Aeronautics and Space Administration under the Exoplanet Exploration Program. The authors wish to recognize and acknowledge the very significant cultural role and reverence that the summit of Maunakea has always had within the Native Hawaiian community. We are most fortunate to have the opportunity to conduct observations from this mountain.

C.A.C. and S.P.H. acknowledge that this research was carried out at the Jet Propulsion Laboratory, California Institute of Technology, under a contract with the National Aeronautics and Space Administration (80NM0018D0004).

L.M.B acknowledges the support of the European Union's Horizon Europe Framework Programme under the Marie Skłodowska-Curie Actions grant agreement No. 101086149 (EXOWORLD).

WIYN is a joint facility of the University of Wisconsin-Madison, Indiana University, NSF's NOIRLab, the Pennsylvania State University, Purdue University, the University of California-Irvine, and the University of Missouri. The authors are honored to be permitted to conduct astronomical research on Iolkam Du'ag (Kitt Peak), a mountain with particular significance to the Tohono O'odham. Data presented herein were obtained at the WIYN Observatory from telescope time allocated to NN-EXPLORE (PI: Gupta; 2022A-665981, 2022B-936991, 2023A-845810, PI: Kanodia; 2023B-438370, 2024A-103024) through the scientific partnership of NASA, the NSF, and NOIRLab.

Deepest gratitude to Zade Arnold, Joe Davis, Michelle Edwards, John Ehret, Tina Juan, Brian Pisarek, Aaron Rowe, Fred Wortman, the Eastern Area Incident Management Team, and all of the firefighters and air support crew who fought the recent Contreras fire. Against great odds, you saved the Kitt Peak National Observatory.

Some of the observations in this paper made use of NESSI. NESSI was funded by the NASA Exoplanet Exploration Program and the NASA Ames Research Center. NESSI was built at the Ames Research Center by Steve B. Howell, Nic Scott, Elliott P. Horch, and Emmett Quigley.

Some of the observations in the paper made use of the High-Resolution Imaging instrument(s) 'Alopeke. 'Alopeke was funded by the NASA Exoplanet Exploration Program and built at the NASA Ames Research Center by Steve B. Howell, Nic Scott, Elliott P. Horch, and Emmett Quigley. 'Alopeke was mounted on the Gemini-North (and/or South) telescope of the international Gemini Observatory, a program of NSF NOIRLab, which is managed by the Association of Universities for Research in Astronomy (AURA) under a cooperative agreement with the U.S. National Science Foundation on behalf of the Gemini Observatory partnership: the U.S. National Science Foundation (United States), National Research Council

(Canada), Agencia Nacional de Investigación y Desarrollo (Chile), Ministerio de Ciencia, Tecnología e Innovación (Argentina), Ministério da Ciência, Tecnologia, Inovações e Comunicações (Brazil), and Korea Astronomy and Space Science Institute (Republic of Korea).

The University of Chicago group acknowledges funding for the MAROON-X project from the David and Lucile Packard Foundation, the Heising-Simons Foundation, the Gordon and Betty Moore Foundation, the Gemini Observatory, the NSF (award No. 2108465), and NASA (grant number 80NSSC22K0117). The Gemini observations are associated with program GN-2023B-Q-104 (PI: Kanodia).

This material is based upon work supported by the National Science Foundation Graduate Research Fellowship under grant No. DGE 1746045.

This work has made use of data from the European Space Agency (ESA) mission Gaia (https://www.cosmos.esa.int/gaia), processed by the Gaia Data Processing and Analysis Consortium (DPAC; https://www.cosmos.esa.int/web/gaia/dpac/consortium). Funding for the DPAC has been provided by national institutions, in particular, the institutions participating in the Gaia Multilateral Agreement.

Some of the observations in this paper were obtained with the Samuel Oschin Telescope 48 inch and the 60 inch telescope at the Palomar Observatory as part of the ZTF project. ZTF is supported by the NSF under grant No. AST-2034437 and a collaboration including Caltech, IPAC, the Weizmann Institute for Science, the Oskar Klein Center at Stockholm University, the University of Maryland, Deutsches Elektronen-Synchrotron and Humboldt University, the TANGO Consortium of Taiwan, the University of Wisconsin at Milwaukee, Trinity College Dublin, Lawrence Livermore National Laboratories, and IN2P3, France. Operations are conducted by COO, IPAC, and UW.

Computations for this research were performed on the Pennsylvania State University's Institute for Computational and Data Sciences Advanced Cyberinfrastructure (ICDS-ACI). This content is solely the responsibility of the authors and does not necessarily represent the views of the ICDS.

The Center for Exoplanets and Habitable Worlds is supported by the Pennsylvania State University, the Eberly College of Science, and the Pennsylvania Space Grant Consortium.

Some of the data presented in this paper were obtained from MAST at STScI. Support for MAST for non-Hubble Space Telescope data is provided by the NASA Office of Space Science via grant NNX09AF08G and by other grants and contracts.

This work includes data collected by the TESS mission, which are publicly available from MAST. Funding for the TESS mission is provided by the NASA Science Mission directorate. This research made use of the (i) NASA Exoplanet Archive, which is operated by Caltech, under contract with NASA under the Exoplanet Exploration Program, (ii) SIMBAD database, operated at CDS, Strasbourg, France, (iii) NASA's Astrophysics Data System Bibliographic Services, and (iv) data from 2MASS, a joint project of the University of Massachusetts and IPAC at Caltech, funded by NASA and the NSF.

This research has made use of the SIMBAD database, operated at CDS, Strasbourg, France, and NASA's Astrophysics Data System Bibliographic Services.

This research has made use of the Exoplanet Follow-up Observation Program website, which is operated by the California Institute of Technology, under contract with the National Aeronautics and Space Administration under the Exoplanet Exploration Program

C.I.C. acknowledges support by an appointment to the NASA Postdoctoral Program at the Goddard Space Flight Center, administered by USRA through a contract with NASA.

Facilities: Gaia, HET (HPF), WIYN 3.5 m (NESSI), Shane (ShARCS), Gemini-N (MAROON-X), Gemini-N ('Alopeke), Palomar AO (PHARO), 1.2 m FLWO (KeplerCam), Swope 1.0 m, RBO, Keeble, LCOGT 0.4 m Teide, ZTF, TESS, K2, LCRO 0.3 m, Exoplanet Archive.

Software: `ArviZ` (R. Kumar et al. 2019), AstroImageJ (K. A. Collins et al. 2017), `astrometry.net` (D. W. Hogg et al. 2008), `astroquery` (A. Ginsburg et al. 2019), `astropy` (T. P. Robitaille et al. 2013; Astropy Collaboration et al. 2018), BANYAN (J. Gagne et al. 2018), BANZAI (C. McCully et al. 2018), `barycorrpy` (S. Kanodia & J. Wright 2018), `celerite2` (D. Foreman-Mackey et al. 2017; D. Foreman-Mackey 2018), `DEATHSTAR` (G. Ross et al. 2024), `eleanor` (A. D. Feinstein et al. 2019), `EVEREST` (R. Luger et al. 2016, 2018), `EXOFAST v2` (J. D. Eastman 2017), `exoplanet` (D. Foreman-Mackey et al. 2021a, 2021b), `HPF-SpecMatch` (G. Stefansson et al. 2020), `HxRGproc` (J. P. Ninan et al. 2018), `Galpy` (J. Bovy 2015), `iPython` (F. Perez & B. E. Granger 2007), `lightkurve` (Lightkurve Collaboration et al. 2018), `matplotlib` (J. D. Hunter 2007), `MOLUSC` (M. L. Wood et al. 2021), `NumPy` (T. Oliphant 2006), `pandas` (W. McKinney 2010), `photutils` (L. Bradley et al. 2020), `pyastrotools` (S. Kanodia 2023), `PyMC3` (J. Salvatier et al. 2016), `scipy` (T. E. Oliphant 2007; P. Virtanen et al. 2020), `SERVAL` (M. Zechmeister et al. 2018), `tglc` (T. Han & T. D. Brandt 2023), `Theano` (The Theano Development Team et al. 2016), `TRICERATOPS` (S. Giacalone & C. D. Dressing 2020; S. Giacalone et al. 2021).

ORCID iDs

Shubham Kanodia https://orcid.org/0000-0001-8401-4300
Arvind F. Gupta https://orcid.org/0000-0002-5463-9980
Caleb I. Cañas https://orcid.org/0000-0003-4835-0619
Lia Marta Bernabò https://orcid.org/0000-0002-8035-1032
Varghese Reji https://orcid.org/0009-0006-7298-619X
Te Han https://orcid.org/0000-0002-7127-7643
Madison Brady https://orcid.org/0000-0003-2404-2427
Andreas Seifahrt https://orcid.org/0000-0003-4526-3747
William D. Cochran https://orcid.org/0000-0001-9662-3496
Nidia Morrell https://orcid.org/0000-0003-2535-3091
Ritvik Basant https://orcid.org/0000-0003-4508-2436
Jacob Bean https://orcid.org/0000-0003-4733-6532
Chad F. Bender https://orcid.org/0000-0003-4384-7220
Zoë L. de Beurs https://orcid.org/0000-0002-7564-6047
Allyson Bieryla https://orcid.org/0000-0001-6637-5401
Nina Brown https://orcid.org/0009-0003-1142-292X
Franklin Chapman https://orcid.org/0009-0003-9699-1063
David R. Ciardi https://orcid.org/0000-0002-5741-3047
Catherine A. Clark https://orcid.org/0000-0002-2361-5812
Ethan G. Cotter https://orcid.org/0009-0003-1637-8315
Scott A. Diddams https://orcid.org/0000-0002-2144-0764
Samuel Halverson https://orcid.org/0000-0003-1312-9391

Suzanne Hawley https://orcid.org/0000-0002-6629-4182
Leslie Hebb https://orcid.org/0000-0003-1263-8637
Rae Holcomb https://orcid.org/0000-0002-5034-9476
Steve B. Howell https://orcid.org/0000-0002-2532-2853
Henry A. Kobulnicky https://orcid.org/0000-0002-4475-4176
Adam F. Kowalski https://orcid.org/0000-0001-7458-1176
Alexander Larsen https://orcid.org/0000-0002-2401-8411
Jessica Libby-Roberts https://orcid.org/0000-0002-2990-7613
Andrea S. J. Lin https://orcid.org/0000-0002-9082-6337
Michael B. Lund https://orcid.org/0000-0003-2527-1598
Rafael Luque https://orcid.org/0000-0002-4671-2957
Andrew Monson https://orcid.org/0000-0002-0048-2586
Joe P. Ninan https://orcid.org/0000-0001-8720-5612
Brock A. Parker https://orcid.org/0000-0001-9307-8170
Gabrielle Ross https://orcid.org/0009-0006-7023-1199
Arpita Roy https://orcid.org/0000-0001-8127-5775
Christian Schwab https://orcid.org/0000-0002-4046-987X
Guðmundur Stefánsson https://orcid.org/0000-0001-7409-5688
Andrew Vanderburg https://orcid.org/0000-0001-7246-5438

References

Agol, E., Luger, R., & Foreman-Mackey, D. 2020, AJ, 159, 123
Albrecht, S. H., Dawson, R. I., & Winn, J. N. 2022, PASP, 134, 082001
Alibert, Y., Mordasini, C., Benz, W., & Winisdoerffer, C. 2005, A&A, 434, 343
Anglada-Escude, G., & Butler, R. P. 2012, ApJS, 200, 15
Astropy Collaboration, Price-Whelan, A. M., Sipőcz, B. M., et al. 2018, AJ, 156, 123
Bailer-Jones, C. A. L., Rybizki, J., Fouesneau, M., Demleitner, M., & Andrae, R. 2021, AJ, 161, 147
Banerjee, B., Narang, M., Manoj, P., et al. 2024, AJ, 168, 7
Bernabò, L. M., Kanodia, S., Canas, C. I., et al. 2024, arXiv:2409.16889
Bovy, J. 2015, ApJS, 216, 29
Bradley, L., Sipőcz, B., Robitaille, T., et al. 2020, astropy/photutils: v1.0.0, Zenodo, doi:10.5281/zenodo.4044744
Brasser, R., Matsumura, S., Ida, S., Mojzsis, S. J., & Werner, S. C. 2016, ApJ, 821, 75
Brown, T. M., Baliber, N., Bianco, F. B., et al. 2013, PASP, 125, 1031
Bryant, E. M., Bayliss, D., & Van Eylen, V. 2023, MNRAS, 521, 3663
Cañas, C. I., Kanodia, S., Bender, C. F., et al. 2022, AJ, 164, 50
Cañas, C. I., Kanodia, S., Libby-Roberts, J., et al. 2023, AJ, 166, 30
Cañas, C. I., Stefansson, G., Kanodia, S., et al. 2020, AJ, 160, 147
Chambers, K. C., Magnier, E. A., Metcalfe, N., et al. 2017, yCat, II/349
Choi, J., Dotter, A., Conroy, C., et al. 2016, ApJ, 823, 102
Ciesla, F. J., Mulders, G. D., Pascucci, I., & Apai, D. 2015, ApJ, 804, 9
Collins, K. A., Kielkopf, J. F., Stassun, K. G., & Hessman, F. V. 2017, AJ, 153, 77
Cutri, R. M., Skrutskie, M. F., van Dyk, S., et al. 2003, The IRSA 2MASS All-Sky Point Source Catalog, NASA/IPAC, http://irsa.ipac.caltech.edu/applications/Gator/
Dawson, R. I., & Johnson, J. A. 2018, ARA&A, 56, 175
Dawson, R. I., & Murray-Clay, R. A. 2013, ApJL, 767, L24
Dekany, R., Roberts, J., Burruss, R., et al. 2013, ApJ, 776, 130
Delamer, M., Kanodia, S., Cañas, C. I., et al. 2024, ApJ, 962, L22
Dotter, A. 2016, ApJS, 222, 8
Dressing, C. D., Vanderburg, A., Schlieder, J. E., et al. 2017, AJ, 154, 207
Eastman, J., Siverd, R., & Gaudi, B. S. 2010, PASP, 122, 935
Eastman, J. D. 2017, EXOFASTv2: Generalized publication-quality exoplanet modeling code, Astrophysics Source Code Library, ascl:1710.003
El-Badry, K., Rix, H.-W., & Heintz, T. M. 2021, MNRAS, 506, 2269
Espinoza, N., Bayliss, D., Hartman, J. D., et al. 2016, AJ, 152, 108
Feinstein, A. D., Montet, B. T., Foreman-Mackey, D., et al. 2019, PASP, 131, 094502
Foreman-Mackey, D. 2018, RNAAS, 2, 31
Foreman-Mackey, D., Agol, E., Ambikasaran, S., & Angus, R. 2017, AJ, 154, 220
Foreman-Mackey, D., Luger, R., Agol, E., et al. 2021a, JOSS, 6, 3285
Foreman-Mackey, D., Savel, A., Luger, R., et al. 2021b, exoplanet-dev/exoplanet v0.4.4, doi:10.5281/zenodo.1998447
Franceschi, R., Henning, T., Tabone, B., et al. 2024, A&A, 687, A96
Furlan, E., Ciardi, D. R., Everett, M. E., et al. 2017, AJ, 153, 71
Gagne, J., Mamajek, E. E., Malo, L., et al. 2018, ApJ, 856, 23
Gaia Collaboration, Vallenari, A., Brown, A. G. A., et al. 2023, A&A, 674, A1
Gan, T., Wang, S. X., Wang, S., et al. 2023, AJ, 165, 17
Giacalone, S., & Dressing, C. D., 2020 Triceratops: Candidate Exoplanet Rating Tool, Astrophysics Source Code Library, ascl:2002.004
Giacalone, S., Dressing, C. D., Jensen, E. L. N., et al. 2021, AJ, 161, 24
Ginsburg, A., Sipőcz, B. M., Brasseur, C. E., et al. 2019, AJ, 157, 98
Green, G. M., Schlafly, E., Zucker, C., Speagle, J. S., & Finkbeiner, D. 2019, ApJ, 887, 93
Han, T., & Brandt, T. D. 2023, AJ, 165, 71
Hayward, T. L., Brandl, B., Pirger, B., et al. 2001, PASP, 113, 105
Hogg, D. W., Blanton, M., Lang, D., Mierle, K., & Roweis, S. 2008, , 394, 27
Howell, S. B., Everett, M. E., Sherry, W., Horch, E., & Ciardi, D. R. 2011, AJ, 142, 19
Huehnerhoff, J., Ketzeback, W., Bradley, A., et al. 2016, Proc. SPIE, 9908, 99085H
Hunter, J. D. 2007, CSE, 9, 90
Jenkins, J. M., Twicken, J. D., McCauliff, S., et al. 2016, Proc. SPIE, 9913, 99133E
Johnson, D. R. H., & Soderblom, D. R. 1987, AJ, 93, 864
Johnson, J. A., & Apps, K. 2009, ApJ, 699, 933
Jordan, A., Hartman, J. D., Bayliss, D., et al. 2022, AJ, 163, 125
Kanodia, S. 2023, shbhuk/pyastrotools: v0.3, Zenodo, doi:10.5281/zenodo.7685628
Kanodia, S., Cañas, C. I., Mahadevan, S., et al. 2024, AJ, 167, 161
Kanodia, S., Mahadevan, S., Libby-Roberts, J., et al. 2023, AJ, 165, 120
Kanodia, S., Mahadevan, S., Ramsey, L. W., et al. 2018, Proc. SPIE, 10702, 107026Q
Kanodia, S., & Wright, J. 2018, RNAAS, 2, 4
Kasper, D. H., Ellis, T. G., Yeigh, R. R., et al. 2016, PASP, 128, 105005
Kumar, R., Carroll, C., Hartikainen, A., & Martin, O. A. 2019, JOSS, 4, 1143
Kunimoto, M., Daylan, T., Guerrero, N., et al. 2022, ApJS, 259, 33
Lightkurve Collaboration, Cardoso, J. V. D. M., Hedges, C., et al., 2018 Lightkurve: Kepler and TESS time series analysis in Python, Astrophysics Source Code Library, ascl:1812.013
Lin, A. S. J., Libby-Roberts, J. E., Alvarado-Montes, J. A., et al. 2023, AJ, 166, 90
Lissauer, J. J. 2007, ApJ, 660, L149
Livingston, J. H., Crossfield, I. J. M., Petigura, E. A., et al. 2018, AJ, 156, 277
Luger, R., Agol, E., Foreman-Mackey, D., et al. 2019, AJ, 157, 64
Luger, R., Agol, E., Kruse, E., et al. 2016, AJ, 152, 100
Luger, R., Kruse, E., Foreman-Mackey, D., Agol, E., & Saunders, N. 2018, AJ, 156, 99
Mahadevan, S., Ramsey, L., Bender, C., et al. 2012, Proc. SPIE, 8446, 84461S
Mahadevan, S., Ramsey, L. W., Terrien, R., et al. 2014, Proc. SPIE, 9147, 91471G
Mandel, K., & Agol, E. 2002, ApJL, 580, L171
Masci, F. J., Laher, R. R., Rusholme, B., et al. 2019, PASP, 131, 018003
McCully, C., Volgenau, N. H., Harbeck, D.-R., et al. 2018, Proc. SPIE, 10707, 107070K
McKinney, W. 2010, in Proc. of the 9th Python in Science Conf., ed. S. van der Walt & J. Millman (Austin, TX: SciPy), 56
McLaughlin, D. B. 1924, ApJ, 60, 22
Metcalf, A. J., Anderson, T., Bender, C. F., et al. 2019, Optic, 6, 233
Mulders, G. D., Drążkowska, J., van der Marel, N., Ciesla, F. J., & Pascucci, I. 2021, ApJL, 920, L1
NASA Exoplanet Archive 2024, Planetary Systems, v2024-05-15, NExScI-Caltech/IPAC
NExScI 2022, Exoplanet Follow-up Observing Program Web Service, IPAC
Ninan, J. P., Bender, C. F., Mahadevan, S., et al. 2018, Proc. SPIE, 10709, 107092U
Ohno, K., & Fortney, J. J. 2023, ApJ, 956, 125
Oliphant, T. 2006, NumPy: A guide to NumPy., http://www.numpy.org/
Oliphant, T. E. 2007, CSE, 9, 10
Perez, F., & Granger, B. E. 2007, CSE, 9, 21
Petigura, E. A., Crossfield, I. J. M., Isaacson, H., et al. 2018, AJ, 155, 21
Ramsey, L. W., Weedman, D. W., Ray, F. B., & Sneden, C. 1988, in ESO Conf. Workshop Proc., ed. M.-H. Ulrich (Garching: ESO), 119

Raymond, S. N., O'Brien, D. P., Morbidelli, A., & Kaib, N. A. 2009, Icar, 203, 644
Reji, V., Kanodia, S., Ninan, J., et al. 2024, arXiv:2409.01371
Robitaille, T. P., Tollerud, E. J., Greenfield, P., et al. 2013, A&A, 558, A33
Ross, G., Vanderburg, A., de Beurs, Z. L., et al. 2024, MNRAS, 528, 5160
Rossiter, R. A. 1924, ApJ, 60, 15
Salvatier, J., Wiecki, T. V., & Fonnesbeck, C. 2016, PeerJ Comput. Sci., 2, e55
Schonrich, R., Binney, J., & Dehnen, W. 2010, MNRAS, 403, 1829
Scott, N. J., Howell, S. B., Gnilka, C. L., et al. 2021, FrASS, 8, 138
Scott, N. J., Howell, S. B., Horch, E. P., & Everett, M. E. 2018, PASP, 130, 054502
Seager, S., & Mallen-Ornelas, G. 2003, ApJ, 585, 1038
Seifahrt, A., Bean, J. L., Kasper, D., et al. 2022, Proc. SPIE, 12184, 121841G
Seifahrt, A., Bean, J. L., Stürmer, J., et al. 2016, Proc. SPIE, 9908, 990818
Seifahrt, A., Bean, J. L., Sturmer, J., et al. 2020, Proc. SPIE, 11447, 114471F
Smith, J. C., Stumpe, M. C., Van Cleve, J. E., et al. 2012, PASP, 124, 1000
Srinath, S., McGurk, R., Rockosi, C., et al. 2014, Proc. SPIE, 9148, 91482Z
Stassun, K. G., Oelkers, R. J., Pepper, J., et al. 2018, AJ, 156, 102
Stefansson, G., Canas, C., Wisniewski, J., et al. 2020, AJ, 159, 100
Stefansson, G., Hearty, F., Robertson, P., et al. 2016, ApJ, 833, 175
Stefansson, G., Mahadevan, S., Miguel, Y., et al. 2023, Sci, 382, 1031
Stumpe, M. C., Smith, J. C., Catanzarite, J. H., et al. 2014, PASP, 126, 100
Stumpe, M. C., Smith, J. C., Van Cleve, J. E., et al. 2012, PASP, 124, 985
Szentgyorgyi, A. H., Geary, J. G., Latham, D. W., et al. 2005, BAAS, 37, 1339
The Theano Development Team, Al-Rfou, R., Alain, G., et al. 2016, arXiv:1605.02688
Triaud, A. H. M. J., Dransfield, G., Kagetani, T., et al. 2023, MNRAS, 525, L98
van Dishoeck, E. F., Grant, S., Tabone, B., et al. 2023, FaDi, 245, 52
Vanderburg, A., Latham, D. W., Buchhave, L. A., et al. 2016, ApJS, 222, 14
Virtanen, P., Gommers, R., Oliphant, T. E., et al. 2020, NatMe, 17, 261
Wood, M. L., Mann, A. W., & Kraus, A. L. 2021, AJ, 162, 128
Wright, E. L., Eisenhardt, P. R. M., Mainzer, A. K., et al. 2010, AJ, 140, 1868
Wright, J. T., & Eastman, J. D. 2014, PASP, 126, 838
Yee, S. W., Petigura, E. A., & Braun, K. V. 2017, ApJ, 836, 77
Yee, S. W., Winn, J. N., Hartman, J. D., et al. 2022, AJ, 164, 70
Zechmeister, M., Reiners, A., Amado, P. J., et al. 2018, A&A, 609, A12